

## LA-UR-19-21820

Approved for public release; distribution is unlimited.

Title: Investigating the Dynamic Compaction Behavior of Brittle Powders

Author(s): Voorhees, Travis John

Intended for: Graduate thesis proposal

Issued: 2019-03-01

---

**Disclaimer:**

Los Alamos National Laboratory, an affirmative action/equal opportunity employer, is operated by Triad National Security, LLC for the National Nuclear Security Administration of U.S. Department of Energy under contract 89233218CNA000001. By approving this article, the publisher recognizes that the U.S. Government retains nonexclusive, royalty-free license to publish or reproduce the published form of this contribution, or to allow others to do so, for U.S. Government purposes. Los Alamos National Laboratory requests that the publisher identify this article as work performed under the auspices of the U.S. Department of Energy. Los Alamos National Laboratory strongly supports academic freedom and a researcher's right to publish; as an institution, however, the Laboratory does not endorse the viewpoint of a publication or guarantee its technical correctness.

# **INVESTIGATING THE DYNAMIC COMPACTION BEHAVIOR OF BRITTLE POWDERS**

A Dissertation Proposal  
Presented to  
The Academic Faculty

By

Travis J. Voorhees

In Partial Fulfillment  
of the Requirements for the Degree  
Doctor of Philosophy in the  
School of Materials Science and Engineering

Georgia Institute of Technology  
February 2018

# INVESTIGATING THE DYNAMIC COMPACTION BEHAVIOR OF BRITTLE POWDERS

Approved by:

Dr. Naresh Thadhani, *Advisor*  
School of Materials Science and Engineering  
*Georgia Institute of Technology*

Dr. Min Zhou  
School of Mechanical Engineering  
*Georgia Institute of Technology*

Dr. Preet Singh  
School of Materials Science and Engineering  
*Georgia Institute of Technology*

Dr. D. Anthony Fredenburg, *Advisor*  
Applied Theoretical Physics, XTD-NTA  
*Los Alamos National Laboratory*

Dr. Kimberly Kurtis  
School of Civil Engineering  
*Georgia Institute of Technology*

Date Approved: February 14, 2018

# TABLE OF CONTENTS

|   |           |
|---|-----------|
| <b>Abstract</b> .....   | <b>1</b>  |
| <b>Chapter 1: Introduction</b> .....  | <b>2</b>  |
| <b>Chapter 2: Historical Efforts to Predict Densification</b> .....                     | <b>4</b>  |
| 2.1. The Shocked State of Homogeneous Solids .....                                      | 4         |
| 2.1.1.Applicability of the Rankine-Hugoniot Relations for Heterogeneous Materials ..... | 5         |
| 2.1.2.Determining the Shocked State of a Powder .....                                   | 6         |
| 2.1.3.Experimental Diagnostics in Plate-on-Plate Impact Experiments .....               | 8         |
| 2.2. Densification Response of Distended Solids (Powders).....                          | 9         |
| 2.2.1.Equation of State of Powders.....   | 10        |
| 2.2.2. Scattered Experimental Data for Brittle Materials.....                           | 18        |
| <b>Chapter 3: Experimental and Computational Methods</b> .....                          | <b>21</b> |
| 3.1. Research Objectives .....  | 21        |
| 3.2. Choice of Material: Ceria.....   | 22        |
| 3.3. Quasistatic Compaction Curve: Limitation for High Density Compact Geometry.....    | 24        |
| 3.4. Gas Gun Plate Impact Experiments at Georgia Tech.....                              | 25        |
| 3.5. Pulsed Powder Cylindrical Implosion Experiments and Proton Radiography .....       | 27        |
| 3.6. Computational Modeling Using LANL Hydrocode FLAG.....                              | 29        |
| <b>Chapter 4: Preliminary Results and Discussion</b> .....                              | <b>32</b> |
| 4.1. Preliminary Gas Gun Plate-Impact Compaction Experiments.....                       | 32        |
| 4.2. Simulations of Georgia Tech Plate Impact Experiments .....                         | 35        |
| 4.3. PHELIX Compaction Experiments: Simulations and Preliminary Data .....              | 37        |

|   |        |
|---|--------|
| <b>Chapter 5: Proposed Future Work</b> .....                                    | 43     |
| 5.1. Plate Impact Experiments: Density and Particle Morphology Variations ..... | 43     |
| 5.2. Increased Velocity Interferometry Diagnostics: PDV Multiplexing.....       | 44     |
| 5.3. Spatially Resolved PDV Measurements.....                                   | 46     |
| 5.4. Modeling Parametrization and Development .....                             | 47     |
| 5.5. Additional PHELIX Compaction Experiments.....                              | 48     |
| 5.5.1.PHELIX Validation of Impedance Matching Technique for Powders.....        | 48     |
| 5.6. Expected Outcome and Potential Challenges .....                            | 49     |
| 5.7. Timeline.....  | 50     |
| <br><b>References</b> .....   | <br>51 |

# ABSTRACT

The compression of porous materials to full density is a complex physical and mechanical process. Modeling efforts to capture the compaction behavior of distended solids (e.g., porous materials or powders) have produced a variety of compaction models, each functionalized to address specific compaction mechanisms. Of the available models, those suited for high-strain-rate deformation associated with shock loading have generally been developed for ductile materials. Compaction models for brittle materials have only been developed for quasistatic loading conditions. No predictive models currently exist that successfully capture the physical processes and mechanics for shock compaction of brittle distended materials, such as sand and oxide powders.

The primary hindrance in producing a dynamic compaction model for brittle distended materials is the lack of availability of high-fidelity, high-precision shock compaction data for validation. The proposed work is aimed at alleviating this issue by developing a high-precision testing method in combination with high-fidelity analysis methods to accurately and precisely determine the shocked state of an ideal test material, ceria powder, under uniaxial strain dynamic compaction. The measured shock compaction data from these brittle powder experiments is then used in initial computations to design a cylindrically converging shock compaction experiment with in situ time-resolved shocked density measurements, employing proton radiography. The preliminary experimental and computational results obtained from these uniaxial strain dynamic compaction and cylindrically converging shock compaction experiments are presented. An experimental and computational path forwards to predictive model development is then proposed.

# CHAPTER 1

## INTRODUCTION

From the asteroids orbiting our solar system to the soil under our homes, heterogeneous materials make up a majority of the natural world. Currently, the physics of the response of such materials to extreme conditions of high pressure shock loading is not well understood. Consequently, computational modeling efforts have commonly failed to make accurate predictions of how heterogeneous materials will react to such conditions. This is especially true for the shock wave loading of brittle powders.

Over the past few decades, the physics community has proposed a number of physical models that attempt to approximate distended material behavior under compressive loading. Dynamic modeling efforts have been primarily focused on describing the pressure-density behavior of shock compressed ductile powders, which deform through different physical mechanisms than brittle powders. Such models do not accurately predict how brittle powders behave under dynamic compression. Hence, there exists a need to develop accurate predictive models for the dynamic compaction of brittle powders, validated against high-precision experiments employing robust time-resolved diagnostic methods.

One of the greatest hurdles facing the development of predictive models for brittle powders is the lack of robust, high-precision shock compaction data available. Currently, the high-fidelity compaction data that is available commonly display uncertainties greater than  $\pm 5\%$ , with some measurements yielding uncertainties as large as  $\pm 50\%$ . Additionally, minimal data is available in the pressure region below full compaction for brittle powders. Accurate, predictive dynamic compaction models for brittle powders cannot be developed until high-precision, high-fidelity shock compaction data are generated.



The focus of the current work is to develop a physical model that accurately predicts the dynamic compaction behavior of brittle powders. As such, the main objectives of this research are:

1. To produce high-fidelity, high-precision shock Hugoniot data for a brittle powder under uniaxial strain dynamic compaction
2. To develop and calibrate a predictive compaction model for brittle powders, validated outside of its one-dimensional calibration region against two-dimensional, unsteady shock loading

The proposed research begins by addressing the historical efforts to predict the response of generally distended materials to compressive loading. The proposed experimental efforts include the approach to generate the high-precision data required to calibrate an accurate compaction model for the shock response of brittle powders. Computational efforts employ the high-precision data experimentally measured to validate proposed compaction models. Progress towards the overall objectives of the proposed research and the timeline for the experimental and computational efforts are presented. An experimental and computational path forwards is proposed, focusing on improving the precision and fidelity of shock measurements.

## **CHAPTER 2**

### **HISTORICAL EFFORTS TO PREDICT DENSIFICATION**

The objective of the proposed research is to accurately predict the dynamic compaction behavior of brittle powders. Predictive modeling for such a class of materials requires a fundamental understanding of the physical compaction mechanisms investigated in prior works and their limitations. As such, this chapter will focus on defining the currently available predictive and descriptive models for the dynamic compression of powders, beginning with the modeling of shock propagation in solid, monolithic materials.

#### **2.1. The Shocked State of Homogeneous Solids**

A shock wave is a type of a mechanical wave characterized as a discontinuous jump in stress and compression level [1, 2]. The ability to predict how shock waves interact with materials has become a prominent area of materials physics research, with applications ranging from cancer therapies [3] to national security [4]. Over the past few decades, comprehensive research efforts have determined the fundamental phenomena governing the shock compression of solid, homogeneous materials, making it possible to accurately predict the behavior of generally homogeneous materials under shock compression as a function of material properties [1, 2].

The propagation of a shock wave through a solid, homogeneous material is often described by the Rankine-Hugoniot (RH) conservation equations, which describe the thermodynamic state of a material across a discontinuous, planar shock front [1, 2]. These conservation equations are developed by applying the RH jump conditions to the one-dimensional (1D) Euler conservation equations of mass, momentum, and energy, resulting in the following relations [5]:

$$\rho_0 U_S = \rho(U_S - U_P) \quad (1)$$

$$P - P_0 = \rho_0 U_S U_P \quad (2)$$

$$E - E_0 = \frac{1}{2}(P + P_0)(V - V_0) \quad (3)$$

Where  $V$  is specific volume,  $U_S$  is shock velocity,  $U_P$  is particle velocity,  $P$  is pressure,  $\rho$  is density,  $E$  is internal energy, and the subscript "0" indicates the undisturbed state of the material. It is important to note that the RH jump conditions assume that the propagating shock wave is of infinitesimal thickness, thereby modeling the wave front as a perfect discontinuity in the material [2, 1]. Although not physically possible in reality, this assumption has been experimentally proven to be a reasonable approximation for strong shock waves propagating in solid, homogeneous materials, as these materials typically exhibit rise times on the order of a few nanoseconds [1]. Additionally, the 1D Euler conservation equations have been developed to model adiabatic flow in inviscid fluids [5]. The RH conservation equations thus assume that modeled materials behave as inviscid fluids. Although valid for solid, homogeneous materials at sufficiently high pressures, this hydrodynamic assumption fails to capture the behavior of many real materials.

### 2.1.1. Applicability of the Rankine-Hugoniot Relations for Heterogeneous Materials

Heterogeneous materials, such as powders, typically do not conform to hydrodynamic assumptions. These materials exhibit wave rise times ranging from tens of nanoseconds [6, 7, 8, 9] to microseconds [10] under shock compression and commonly exhibit non-negligible shear strengths in the low pressure regime. As a result, the RH conservation equations are only able to make a first-order approximation of the bulk thermodynamic state of a shocked powder.

The RH conservation equations utilize a continuum approximation. This approximation homogenizes a material, isotropically distributing material properties and effectively modeling

powders as solid analogues of expanded gases [11]. This precludes any approximation of localized mesoscale phenomena occurring in the bulk material. As it is often the case for heterogeneous materials that bulk material response is dictated by localized mesoscale phenomena, application of the RH conservation equations to calculate the shocked state of heterogeneous materials may propagate significant uncertainties into calculated values [12, 11].

### 2.1.2. Determining the Shocked State of a Material

A large majority of the dynamic compression data produced in shock compression research has been determined using the impedance matching technique [1, 2, 13, 9]. This technique requires researchers to only measure three independent experimental variables. Once these experimental variables are determined, the complete thermodynamic state of the shocked material can be calculated using the RH conservation equations. An example of an impedance matching calculation is shown graphically in **Figure 2.1.** for an asymmetric plate-on-plate impact of materials A and B.

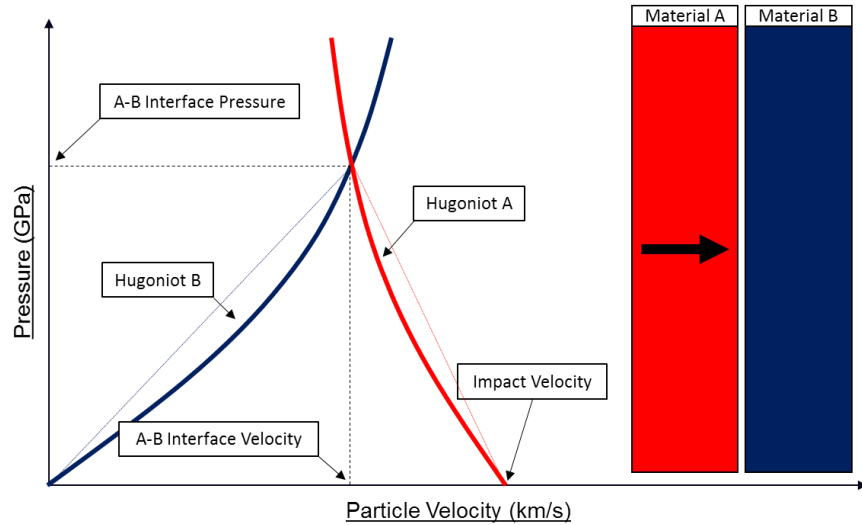


**Figure 2.1.** Example of impedance matching calculation determining interface pressure and velocity for material A impacting material B. The A-B interface pressure and velocity is determined at the intersection of material Hugoniots.

In **Figure 2.1.**, material A is initially moving at impact velocity and material B is stationary in Eulerian coordinates. Upon impact, both material A and B increase in pressure as a function of changes in particle velocity. This pressure-particle velocity trend is defined by the RH conservation of momentum (Eqn. 2), and is commonly referred to as the material Hugoniot [1, 2]. At the A-B interface, the pressure and particle velocity of the two materials must be equal [1, 2]. Thus, the intersection of these two Hugoniot plots yields the shock pressure and particle velocity at the A-B interface. Using this technique, the experimentally measureable parameters of initial density, impact velocity, interface velocity, and shock velocity may be used to calculate the pressure and particle velocity of a shocked material. However, it is important to note that because the impedance matching technique requires that the RH conservation equations be valid for the material tested, impedance matching can only give a first order approximation for the shocked state of heterogeneous materials, such as powders. A common experimental method used to generate the experimental shock compression data used in impedance matching calculations is plate-on-plate impact [2, 1].

Shock compression can be highly complex. In order to reduce complexity and simplify analysis, shock compression studies often investigate 1D shock loading paths. These 1D experiments are commonly performed via plate-on-plate impact [1, 2]. This experimental method drives a planar shock wave across a material via the impact of two planar and parallel surfaces. An idealized diagram of a plate-on-plate impact experiment is presented in **Figure 2.2**, showing a propagating shock wave interacting with a material interface. Using this experimental geometry, interface velocities, shock arrival times, and shock stresses may be measured for use in impedance matching calculations.

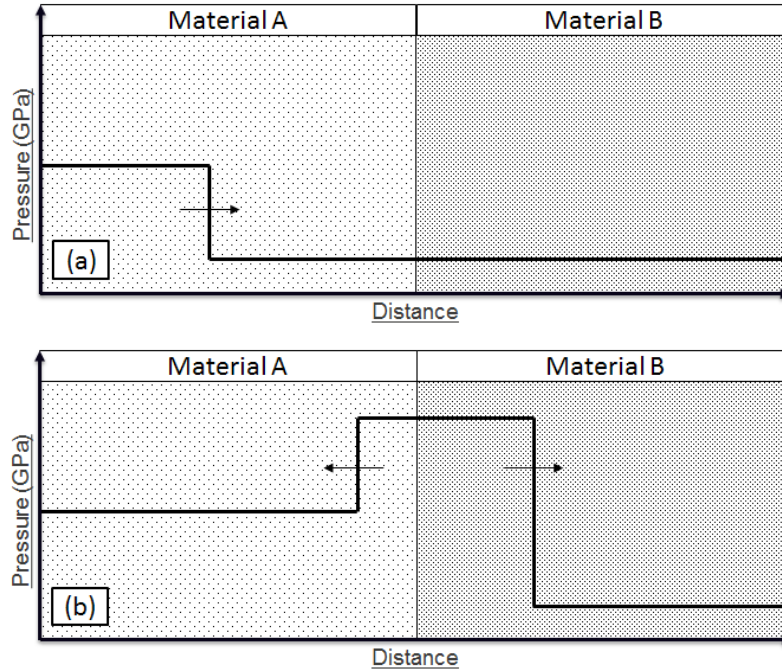


**Figure 2.2.** Pressure-distance diagram illustrating the propagation of an ideal shock wave across a material interface at two time intervals: (a) before and (b) after the propagating shock wave crosses the A-B interface. In this example, material B has a higher shock impedance than material A, increasing the shock pressure across the interface.

### 2.1.3. Experimental Diagnostics in Plate-on-Plate Impact Experiments

A variety of experimental diagnostics have been employed to measure the dynamic responses of materials under 1D shock compression via plate impact. The most popular techniques are the use of flash gaps and contact pins, quartz gauges, embedded gauge packages, and laser interferometry. Initial shock studies utilized flash gaps and contact pins, which were able to measure the arrival and exit times of a shock wave as it propagated through a test material [14]. However, this measurement method reveals no information about the evolution of the shock wave as it transmits through the material. Additionally, the data collected is subject to systematic uncertainties greater than  $\sim 1\%$  due to variations in flash gap closing times [14]. An early alternative to flash gaps and contact pins was the use of quartz gauges [15, 13].

Quartz gauges measure both the transmission and evolution of shock waves as they propagate through a test material by directly measuring the stress state of a quartz gauge in contact with the test

material. However, quartz gauges produced large systematic errors due to measurement rise times on the order of tens of nanoseconds [9]. In an effort to improve temporal resolution, subsequent studies utilized embedded gauge packages such as piezoelectric [16] and piezoresistive [10, 17] stress gauges, which can create or modulate an electrical signal. In theory, these gauges offer high temporal resolution because they produce signals that are a function of changes in material lattice. In practice, these gauges produce significant systematic errors because they are embedded in the test material. As such, shock waves must transit through the embedded gauge, which is commonly a package of materials spanning tens to hundreds of microns in thickness and not impedance matched to the test material [9, 18, 10]. This causes complex wave interactions at gauge package-test material interfaces and ringing in the test material. Many modern shock compaction studies therefore use laser interferometry to measure the shock response of materials.

Laser interferometry has the advantage of being a zero contact measurement technique, allowing cross-timed measurements of interface velocities in a test material without interfering or interacting with the propagating shock wave [19, 20, 21]. Using laser interferometry, shock studies are able to measure unpolluted shock and particle velocities, and determine the thermodynamic state of the test material through impedance matching.

## **2.2 Densification Response of Distended Solids (Powders)**

Real distended materials are intrinsically heterogeneous, exhibiting localized areas of varying impedance during shock compaction. These localized variations can steer shock waves along preferential routes, such as particle contact points, rerouting transmission paths from an originally 1D path to a microstructurally dependent path [22, 18]. **Figure 2.3** shows a 2D mesoscale simulation conducted by Eakins and Thadhani [18], which illustrates the dispersion behavior of an initially planar shock wave as it propagates through a nickel-aluminum powder compact.

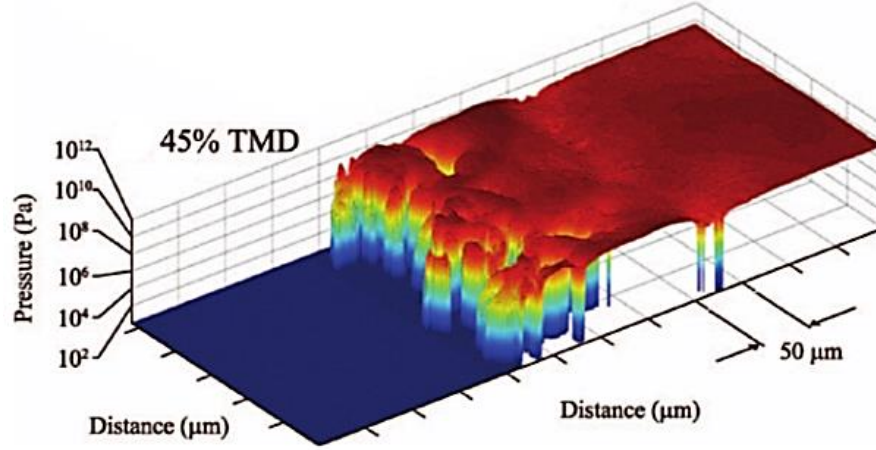


**Figure 2.3.** 2-D mesoscale simulation of shock propagation in a 45% TMD nickel-aluminum powder compact. This surface plot shows shock front dispersion as an initially planar shock wave propagates along preferential routes in the heterogeneous material.

Although it is impossible to induce purely 1D shock loading in a heterogeneous material, plate impact experiments are often used to study their shock compaction response under uniaxial strain dynamic (shock) loading. A first order approximation of the uniaxial strain behavior of a powder is then used to calculate the shocked state employing the RH conservation equations. Attempts to model the dynamic compaction behavior of powders are discussed in the following sections.

### 2.2.1. Equation of State of Powders

Approximations of an equation of state (EOS) for powders have been largely focused on the use of compaction models [23, 24]. These models attempt to derive the thermodynamic state of powdered and porous materials from the thermodynamic state of their fully solid form [25]. In the following, the development, use, and limitations of three compaction models are presented.

#### The $P$ - $\sigma_y$ Model

Originally developed to model the quasistatic compaction behavior of ductile powders, the  $P$ - $\sigma_y$  model attempts to determine densification trends as a function of increasing particle-particle contact area [24, 26]. During compression, the pressure required to densify an initially distended material increases



with increasing density. Examples of this trend are shown in **Figure 2.4**, a density-pressure quasistatic compression curve produced by Fischmeister for iron and alumina powders [27]. In an effort to model this behavior, Fischmeister and Arzt [24, 26] postulated that this increase in resistance to densification can be attributed to the growth of particle-particle contact areas that occur as particles deform into one another. To model the densification mechanism, they divided the compaction process into three stages: particle rearrangement, unconstrained compaction, and constrained compaction. The first stage, particle rearrangement, is the translation of powder particles from their original locations to void spaces under low stresses [26]. Rearrangement usually occurs until a powder compact density reaches the jamming limit, the point at which nearly all voids have been occupied by rearranged particles [26, 28]. Once compact density increases beyond the jamming limit, particle deformation becomes the primary mechanism of compaction [26]. The particle deformation process is illustrated in **Figure 2.5**, and is defined as either unconstrained compaction or constrained compaction.

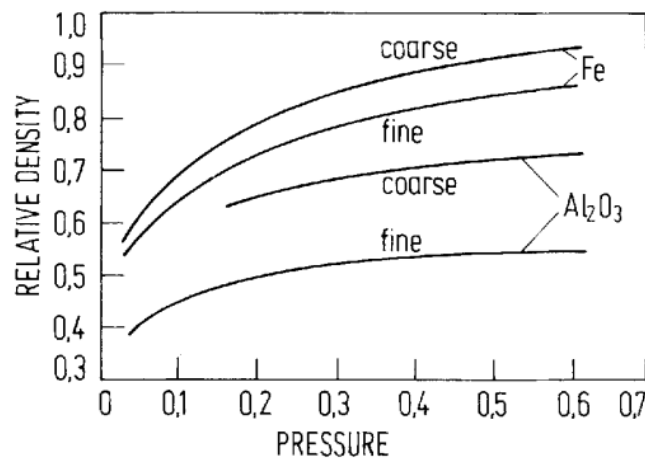


**Figure 2.4.** Quasistatic densification curves for iron and alumina powders of two particle sizes, produced by Fischmeister [27]. As the porous material densifies, the force required to further densify the material increases.

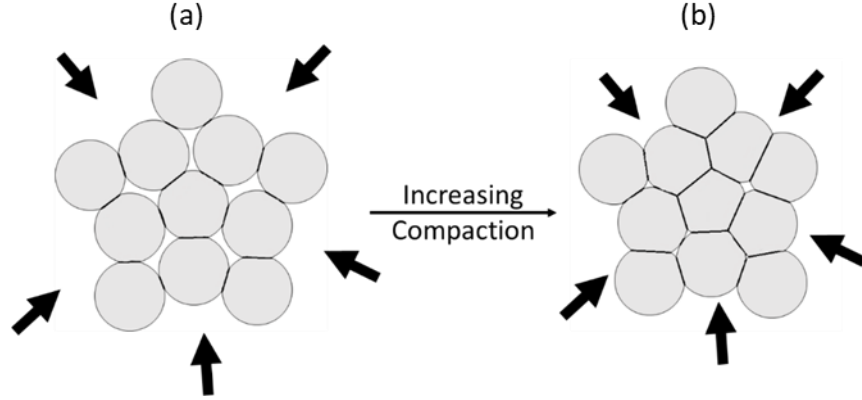


**Figure 2.5.** The latter two stages of powder compaction modeled by Fischmeister and Arzt: (a) unconstrained compaction, where particle-particle contacts are formed by only two particles, and (b) constrained compaction, where particle-particle contact areas begin to intersect with one another and may be formed by more than two particles.

In unconstrained compaction, particle-particle contact areas are circular regions formed as two particles deform into one another. Fischmeister and Arzt [26] defined the pressure,  $P_s$ , required to compact the powder to a density,  $\rho$ , in the unconstrained (soft) compaction regime as:

$$P_s(\rho) = \frac{3}{4\pi} \left( \frac{a(\rho)Z(\rho)}{R^2} \right) \rho \sigma_y(\rho) \quad (4)$$

Where  $a$  is the average particle-particle contact area,  $Z$  is the coordination number of particles,  $R$  is the particle radius, and  $\sigma_y$  is the yield strength of particle-particle contacts. As pressure increases and particles push closer together, the contact areas grow in size. Further growth causes contact areas to impinge upon one another as the void space between particles lessens to a point at which particle-particle contact areas impinge upon the growth of one another, typically around 90% of full density. In this regime, the densification process is referred to as constrained compaction and can be defined using a logarithmic interpolation function [26]:

$$P_H(\rho) = k \sigma_y \ln \left( \frac{a(1)Z(1)}{a(1)Z(1) - a(\rho)Z(\rho)} \right) \quad (5)$$

In Eqn. 5,  $k$  is a constant commonly approximated as 2, and  $a(1)$  and  $Z(1)$  refer to the average particle-particle contact area and coordination number at full density. In order to combine these two stages, Fischmeister and Arzt use a linear combination of  $P_S$  and  $P_H$ , such that [26]:

$$P(\rho) = f_S P_S + f_H P_H \quad (6)$$

Where  $f_S$  and  $f_H$  are the volume fraction of the unconstrained (soft) and constrained (hard) regions in the powder, such that below 90% of full density,  $f_H \approx 0$ , and above 90% of full density,  $f_H$  dominates the response.

The Fischmeister-Arzt model [26] has been shown to be relatively accurate for ductile powders with narrow particle size distributions and particle aspect ratios near 1. However, the model has shown deficiencies when particles are either irregular in shape or brittle in nature [24, 23].

### **The P-P<sub>act</sub> Model**

Developed to model the quasistatic compaction of brittle distended materials, the P-P<sub>act</sub> model by Kenkre and coworkers [29] uses volume-based statistical mechanics to model compaction mechanisms in brittle materials. The mechanisms defining the compaction of brittle, distended materials significantly complicate their compaction process. Brittle materials have minimal ductility and are highly likely to fracture rather than deform when loaded beyond their elastic limits [30]. This causes the compaction process in brittle materials to be primarily dominated by particle fracture and rearrangement. These processes can happen simultaneously at areas of high local stress within a powder compact [26]. A diagram illustrating the mechanism of compaction in brittle powders is presented in **Figure 2.6**.

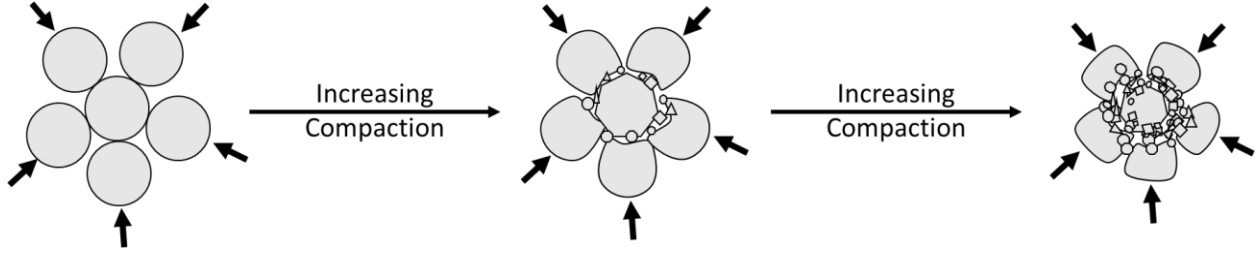


**Figure 2.6.** Diagram of physical mechanism for brittle powder compaction. Brittle powders compact through a combined mechanism of particle fracture and rearrangement.

In an attempt to capture the compaction mechanism of brittle, distended materials, Kenkre and coworkers [29], postulated that the compaction process could be modeled using a form similar to an Arrhenius function. They modified the Arrhenius functional form to be volume-based rather than energy-based, using pressure and volume as conjugate variables rather than the usual energy and temperature [26]. The postulated model divides the compaction process into a non-stress activated and a stress activated region. The non-stress activated region is defined as the initially linear region of the pressure-density curve. The break in linearity of the pressure-density curve is often associated with the onset of particle fracture [26]. As such, the stress-activated region is defined by the initial break in linearity of the pressure-density curve of a material.

In the non-stress activated region, densification is wholly focused on particle rearrangement. Kenkre and coworkers modeled this behavior as a rearrangement probability,  $f_l$ , stating that [26]:

$$f_l = (\text{constant}) \left[ 1 - \exp\left(-\frac{P}{P_l}\right) \right] \quad (7)$$

Where  $P$  is the applied stress and  $P_l$  is the saturation stress at which the linear pressure-density trend breaks. In the stress activated region, densification is dominated by particle fracture and subsequent rearrangement. This region is modeled as a particle overcoming a volume barrier to fill a void. The probability of this occurring is  $f$ , defined as [26]:

$$f = (\text{constant}) \exp\left(\frac{-P_a}{P}\right) \quad (8)$$

Where  $P_a$  is a single pressure barrier and  $P$  is the applied pressure. This Arrhenius-based probability form of compaction model shows good agreement with quasistatic compaction data for brittle powders and is a useful descriptive model [24].

### The P- $\alpha$ Model

One of the most popular compaction models is the P- $\alpha$  compaction model. Originally developed by Herrmann [31] to describe the dynamic compaction of aluminum and iron powders, the P- $\alpha$  compaction model has gained significant traction in the shock compaction community. The model attempts to describe the compaction behavior of distended materials by separating material behavior into elastic and plastic components. Example data using the P- $\alpha$  model for a nickel-titanium mixture is shown in **Figure 2.7**, calculated by Xu and Thadhani [32].

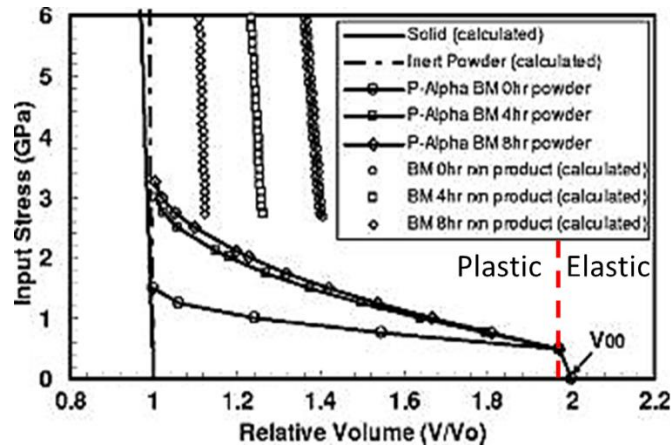


**Figure 2.7.** Pressure-volume curve for the dynamic compaction of nickel-titanium powder mixtures, produced by Xu and Thadhani [32]. The elastic compaction region is defined by the initially linear portion of the compaction curve. The plastic region is then defined as the concave upwards region beyond the discontinuous change in slope.

Herrmann theorized that the equation of state of a porous or distended material can be directly linked to the equation of state of its solid form. In order to link the two forms, Herrmann [31] introduces a distention parameter,  $\alpha$ , such that:

$$\alpha = \frac{V}{V_s} \quad (9)$$

Where,  $V$  is the specific volume of the distended material and  $V_s$  is the specific volume of the same material at full density. Through this definition,  $\alpha$  is the inverse of occupied volume fraction. This model assumes that the material has no shear strength and that the specific internal energy of the distended material is equal to the specific internal energy of its solid form. Through this assumption, it is postulated that the equation of state of a distended material can be solely described as a function of specific volume,  $V_s$ , and internal energy,  $E$ . As such, volume of the distended material may be related to the equation of state of the solid material through the following relation:

$$P = f(V_s, E) = f\left(\frac{V}{\alpha}, E\right) \quad (10)$$

The definition creates a relationship between the volume of the solid material and that of the distended material at a given pressure. Using this general framework, many researchers have proposed functional forms of the P-alpha compaction model. The most prominent functional forms, formatted to calculate the distention parameter  $\alpha$  in the shocked state, are listed in **Table 2.1**.

**Table 2.1.** Comparison of the most prominent P- $\alpha$  functional forms used to predict porous material compaction

| Year | Developer                | Material Modeled                  | $\alpha$ Functional Form  |
|------|--------------------------|-----------------------------------|---|
| 1969 | Herrmann [31]            | Aluminum and iron powders         | $1 + (\alpha_{00} - 1) \left( \frac{P_S - P}{P_S - P_E} \right)^2$  |
| 1969 | Bucher and Karnes [33]   | Iron powder                       | $\alpha_0 + \alpha_1 P + \alpha_2 P^2$  |
| 1970 | Boade [34]               | Copper powder                     | $1 + (\alpha_{00} - 1) \exp[-\bar{\alpha}(P_S - P_E)]$  |
| 1972 | Carrol and Holt [35, 36] | Hollow sphere of ductile material | $\left[ 1 - \exp\left(-\frac{3P}{2\sigma_y}\right) \right]^{-1}$  |
| 1999 | Menikoff and Kober [37]  | Non-equilibrium two-phase flow    | $\left[ 1 - \left( 1 - \frac{1}{\alpha_{00}} \right) \exp\left(-\frac{V_S P_S - V_{00} P_{00}}{V_{00} P_c}\right) \right]^{-1}$ |
| 2007 | Grady [38]               | Sand                              | $\left( \frac{P_S}{P} \right)^{\frac{1}{N}}$  |

In the equations listed in **Table 2.1**,  $\alpha$ ,  $P$ , and  $\sigma_y$  are the distention parameter, pressure, and powder compact yield strength, respectively; the variables  $\alpha_0, \alpha_1, \alpha_2, P_c$ , and  $N$  are fitting constants; and the subscripts "00", "S", "E", refer to the state of the material at initial distention, compression to full density, and compression to the elastic limit, respectively.

### Inability of Compaction Models to Predict Brittle Powder Shock Compaction

Although the currently available compaction models are capable of predicting the dynamic compaction behavior of ductile powders and the quasistatic compaction of ductile and brittle powders, no model is currently capable of fully predicting the dynamic (shock) compaction behavior of brittle powders. This is due to a number of factors including the lack of precision shock compaction data on brittle powders and the common continuum assumptions made in a majority of compaction models which reduce, or entirely preclude, microstructural dependency on compaction behavior.

### 2.2.2. Scattered Experimental Data for Brittle Materials

One of the main challenges in modeling dynamic compaction behavior is the availability of high-fidelity, high-precision shock compaction data, needed for model validation. In order for data to be considered high-fidelity, it must accurately describe the total uncertainty of the measurement, propagating the systematic and random uncertainties of each experimental variable into the total uncertainty. High precision requires that the overall uncertainty be sufficiently low; in the present work, high-precision is arbitrarily defined as a total uncertainty less than  $\pm 2\%$ . Historically, dynamic compaction experiments have produced scattered shock Hugoniot data which either do not display uncertainties [13] or display large uncertainties [10, 39]. The large uncertainties calculated in many brittle compaction experiments are due to a combination of uncertainties propagated through various data collection methods and intrinsic heterogeneities in the microstructures of the powder compacts. Examples of scattered data for sand which fully capture the uncertainties of the experiment are shown in **Figure 2.8** [39, 10]. These data are considered accurate, but not precise. Sand is a highly heterogeneous, brittle, granular material. The intrinsic local heterogeneities of sand cause variances in their compaction behavior, which commonly lead to total uncertainties in calculated shocked states on the order of 10 - 20 % [10, 38, 39].



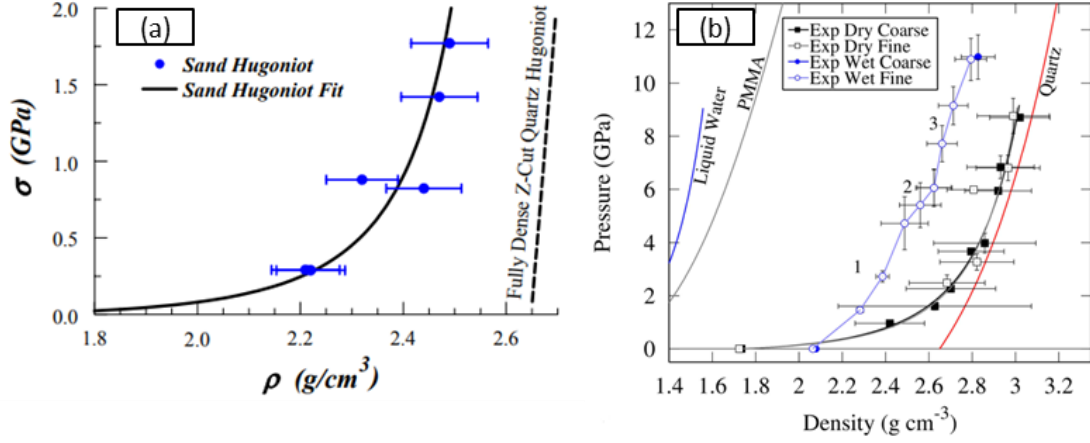


**Figure 2.8:** Examples of scattered pressure-density Hugoniot data with large uncertainties collected for sand. These data were published based on experiments performed by (a) J. L. Brown, et al at Sandia National Labs [39] and (b) J. Lajeunesse, et al at Marquette University [10].

Even if data is high-fidelity, large uncertainties in compaction data limit model development capabilities. In order to develop a compaction model that will accurately determine the compaction behavior of distended materials, highly robust precision shock compaction data is needed. Recently at Los Alamos National Laboratory (LANL), Fredenburg and coworkers [9] have proposed a high-fidelity Hugoniot analysis method in combination with a precision experimental testing method. Using this testing method, low uncertainties ( $\pm 1-8\%$ ) have been reported in the calculated shocked state of ceria powders at two green densities and three particle morphologies [9, 40]. Data collected using this high-fidelity testing method is plotted in **Figure 2.9**. [9, 40].

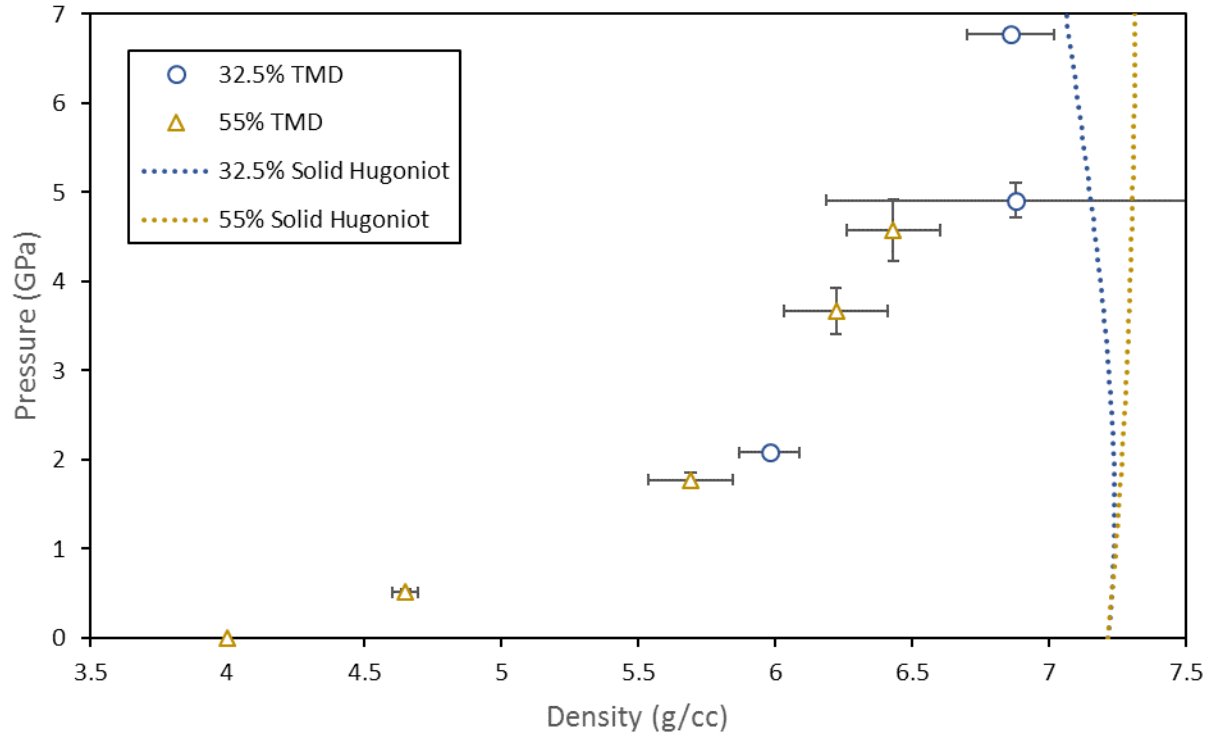


**Figure 2.9.** High fidelity Hugoniot data collected for ceria by D. Fredenburg at LANL [9, 40].

The experimental technique and analysis method proposed by Fredenburg has the ability to produce shock Hugoniot data for brittle powders with high precision and high-fidelity. The proposed work will expand upon this high-fidelity testing method, adapting experimental geometries and diagnostics to further improve measurement precision and fidelity. The experimental and computational methods used in the proposed research to acquire high-fidelity, high-precision data and model brittle powder compaction behavior are described in the next chapter.

## **CHAPTER 3**

### **EXPERIMENTAL AND COMPUTATIONAL METHODS**

This chapter focuses on the technical approach used to gather high-precision, high-fidelity data for a model brittle powder, explaining why and how each experimental method is used. The proposed computational approach to be used in modeling the preceding compaction experiments and determining the best fit compaction models is also discussed. The main focus is on model development and validation, presenting an experimental method for higher dimensional compaction experiments.

#### **3.1. Research Objectives**

The overall objective of this research is to accurately predict the dynamic compaction behavior of brittle, distended materials, validated with precision experiments. As such, the specific objectives of the research are (1) to develop a high-precision experimental method to produce high-fidelity Hugoniot data for a brittle powder material and (2) an improved compaction model for distended materials that captures the compaction mechanisms of brittle materials and is validated through controlled experiments. In order to fulfil these objectives, the following technical approach is used:

1. Select and characterize an ideal powder material with diverse morphological characteristics.
2. Develop and field a robust, high-precision 1D shock compaction testing method employing time-resolved interferometry measurements to gather high-fidelity shock Hugoniot data for the powder material.
3. Calibrate compaction models to the determined shock Hugoniot data, closely matching the particle velocity profiles measured in 1D shock compaction experiments for model validation.
4. Model a 2D shock compaction experiment using the models which most accurately predict 1D particle velocity profiles.

5. Conduct 2D shock compaction experiments with in situ density measurements.
6. Compare data collected from the 2D shock compaction experiment with computational predictions and determine the limitations of compaction models.
7. Improve upon the compaction models to most accurately predict the measured response from 2D shock compaction experiments.

### 3.2. Choice of Material: Ceria

Because of its attractive material properties, ceria is an ideal test material to study the mechanical response of brittle, distended materials to shock loading. Ceria is a lanthanide oxide material that is often used as a glass polishing compound. It is readily available from commercial vendors in a variety of particle sizes with narrow particle size distributions. This makes ceria ideal for studying the effect of powder compact microstructure on the dynamic mechanical behavior of brittle powder compacts. Additionally, it has been shown in previous research [9, 6, 8] that a substantial amount of pressure is required to shock compact ceria powder to near theoretical maximum density (TMD); approximately 12 GPa for compacts with a green density of 55% TMD (4.0 g/cc) [9, 8, 25], which is almost an order of magnitude larger than the 3.5 GPa pressure required to shock compact silica sand to full density [39, 38]. Ceria also has a high density, with a TMD of 7.215 g/cc. The high crush strength and high density of ceria allows a broad range of shock compaction experiments to be performed in the crush region, i.e., experiments which do not fully compact the powder. This broad range improves the potential fidelity of experimental data, allowing more compaction experiments to be completed, making it possible to determine minute differences in the mechanical responses of powder compacts as a function of material properties and microstructure.

Ceria powders of two particle morphologies will be investigated in this work to determine the possible effects of varying microstructures on dynamic compaction behavior. The two particle

morphologies vary in both size and aspect ratio. One powder morphology displays an average particle size on the order of  $1\ \mu\text{m}$  and an equiaxed particle shape; hence forth referred to as “equiaxed” ceria powder in the present work. The particle size distribution for the equiaxed ceria powder and an example SEM image are shown in **Figure 3.1**. The second powder type studied has an average particle size on the order of  $10\ \mu\text{m}$  and a rod-like particle shape; hence forth referred to as “rods” in the present work. Example SEM images of the rods powder are shown in **Figure 3.2**.

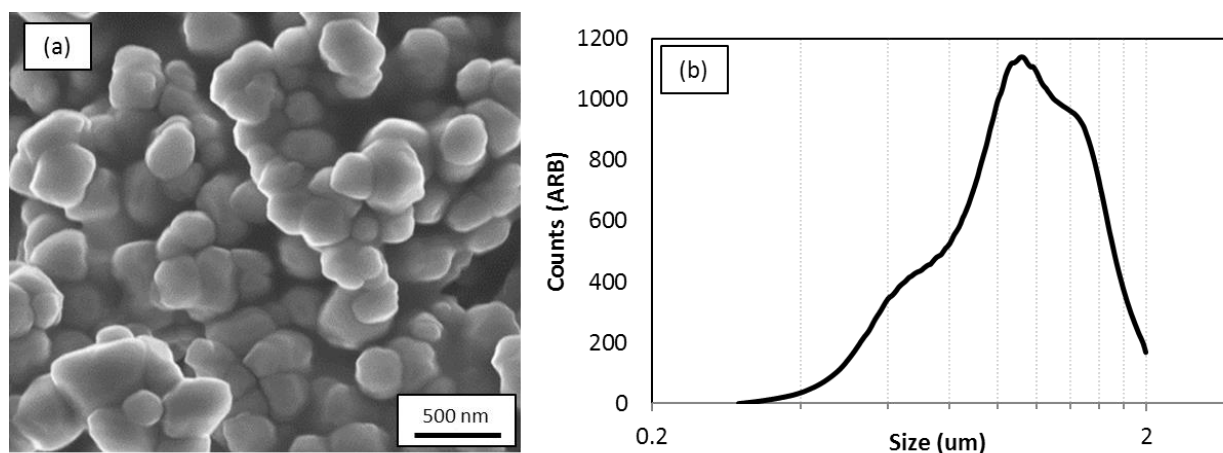


**Figure 3.1.** (a) Example SEM image and (b) particle size distribution for equiaxed ceria powder. SEM image was taken by MST-6 at LANL [41], particle size distribution was measured via disk centrifuge at Georgia Tech.

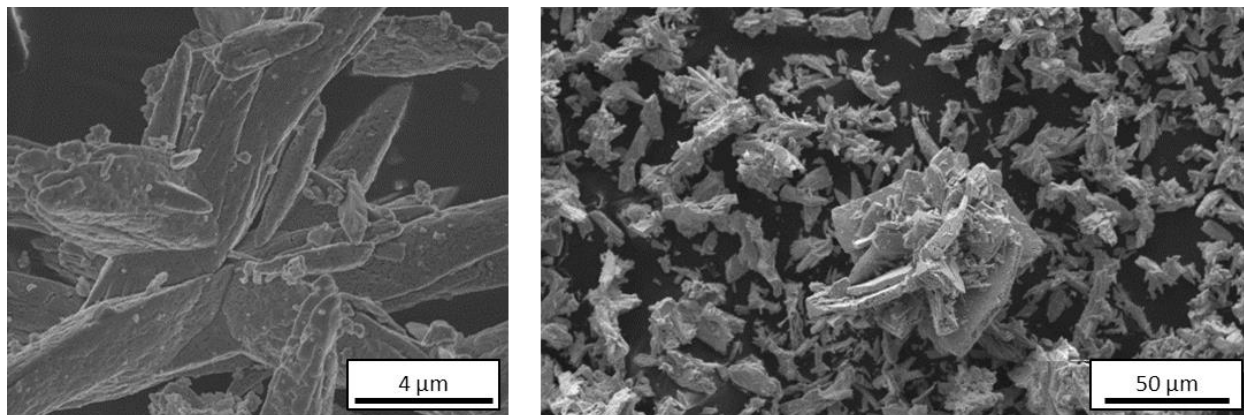


**Figure 3.2.** SEM images of rods ceria powder taken by MST-6 at LANL [41].

### 3.3. Quasistatic Compaction Curve: Limitation for High Density Compact Geometry

In order to both maximize the measureable experimental area and minimize edge effects in plate impact experiments, the diameter of the powder compact must be maximized. Considering the availability of a four-post hydraulic press capable of a 25 ton load, the limiting diameter for making high density powder compacts was defined. The maximum diameter of a high density ceria powder compact was calculated using a quasistatic compaction curve for the two powder morphologies of interest. This curve was created by loading the ceria powder to a step amount of pressure in a punch-and-die set up, then removing the die and measuring the thickness of the powder compact at each step pressure. The quasistatic compaction curve for ceria is shown in **Figure 3.3**. Using this quasistatic compaction curve, it was determined that a high density equiaxed ceria powder compact, approximately 65% TMD, should be obtainable at a diameter of approximately 35 mm using the maximum load of the available hydraulic press at Georgia Tech. With this dimension defined, the first batch of experimental powder capsules were machined with a 34.9 mm (1.375 in) inner diameter. The geometry of the high density powder capsule will be discussed in the next subsection.

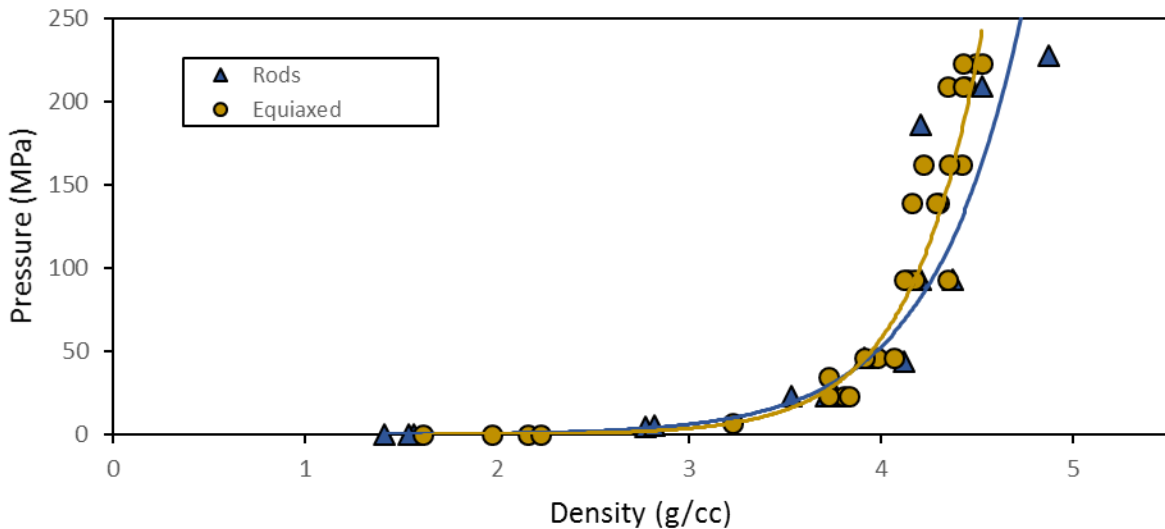


**Figure 3.3.** Quasistatic compaction curve for equiaxed and rods ceria powders. These data were measured at step load increments in a punch and die set up, directly measuring the thickness of the powder compact.

### 3.4. Gas Gun Plate Impact Experiments at Georgia Tech

In the proposed research, 1D plate impact experiments are designed and fielded on ceria powder compacts at Georgia Tech, utilizing the 80 mm light gas gun, shown in **Figure 3.4**.

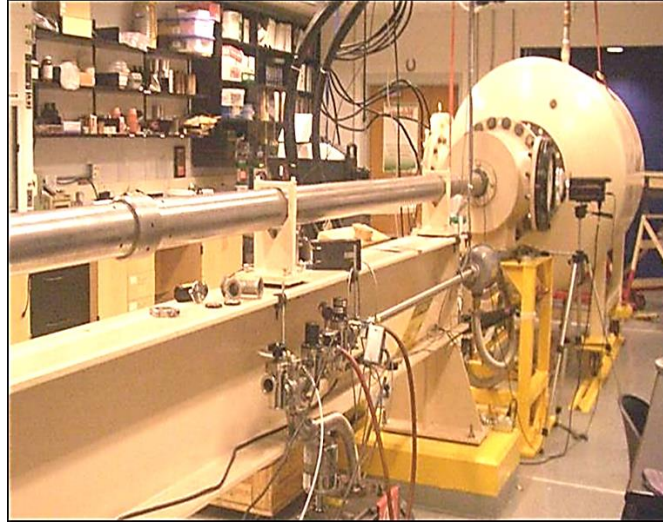


**Figure 3.4.** 80 mm light gas gun barrel leading to experimental chamber available in the Georgia Tech High Strain Rate lab.

The plate impact experiments utilize a powder capsule geometry similar to that used in the work conducted by Fredenburg at LANL [9, 8]. For the experiments at Georgia Tech, the powder capsules are modified to achieve the largest powder compact diameter possible. The CAD drawings for two variations of powder capsules are shown below in **Figure 3.5**, with dimensions listed in **Table 3.1**.

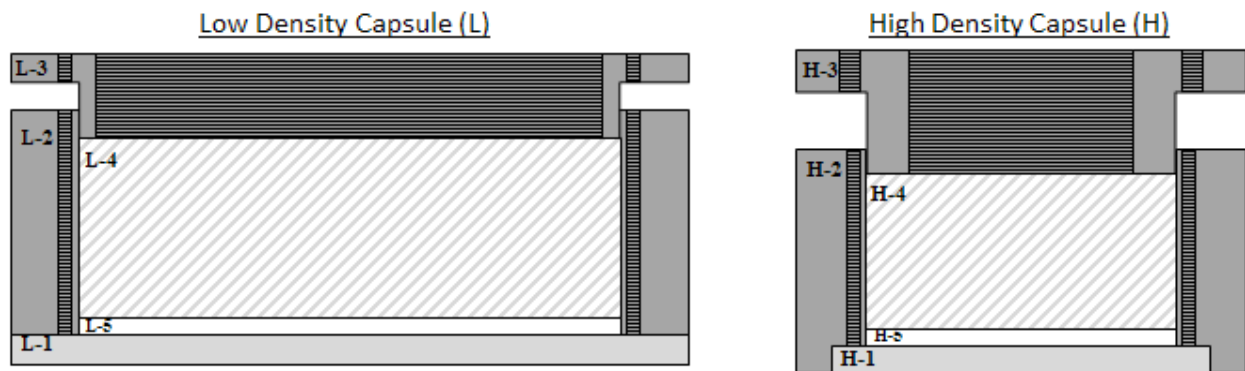


**Figure 3.5.** Scaled longitudinal cross section diagrams of the two powder capsules used in the present research. Part ID definitions and exact dimensions are shown in **Table 3.1**.

**Table 3.1.** Part ID definitions and exact dimensions for the two powder capsules tested.

| ID  | Part Name      | Material         | ID (mm) | OD (mm) | Thickness (mm) |
|-----|----------------|------------------|---------|---------|----------------|
| L-1 | Driver         | OFHC Cu          | N/A     | 76.2    | 3.1            |
| H-1 | Driver         | OFHC Cu          | N/A     | 42.5    | 3.1            |
| L-2 | Cylinder       | Al6061           | 61.0    | 76.2    | 25.4           |
| H-2 | Cylinder       | SS303            | 34.9    | 50.8    | 25.4           |
| L-3 | Retaining Ring | Al6061           | 57.1    | 76.2    | 9.5            |
| H-3 | Retaining Ring | SS303            | 25.4    | 50.8    | 14.3           |
| L-4 | Window         | PMMA             | N/A     | 60.0    | 18             |
| H-4 | Window         | PMMA             | N/A     | 34.0    | 18             |
| L-5 | Powder         | CeO <sub>2</sub> | N/A     | 61.0    | 1.5 - 2.0      |
| H-5 | Powder         | CeO <sub>2</sub> | N/A     | 34.9    | 1.5 - 2.0      |

The large diameter of these powder capsules allows a large real estate for multiple velocity measurements to be fielded. Preliminary plate impact experiments on ceria powder compacts were designed to utilize four Photonic Doppler Velocimetry (PDV) probes and one Velocity Interferometer System for Any Reflector (VISAR) probe to measure the particle velocity, shock velocity, and impact velocity during plate impact experiments. Probe placements for these preliminary experiments are shown in the schematic in **Figure 3.6**.



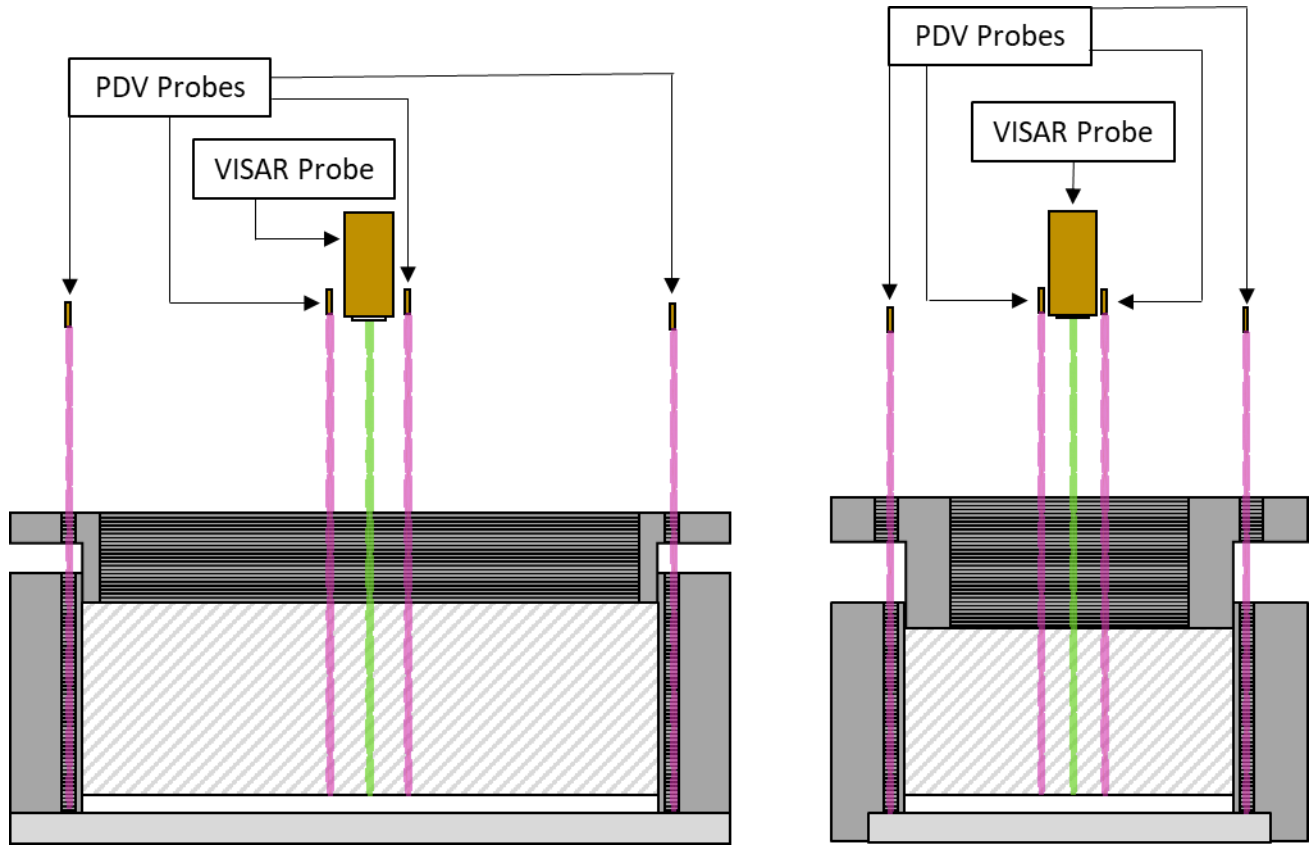


**Figure 3.6.** Velocity probe positions for low density and high density powder capsules. The two outside PDV probes are used to measure tilt and the input wave profile at the copper baseplate rear surface. The inside PDV and VISAR probes are used to measure output wave profile at the ceria-window interface.

### 3.5. Pulsed Power Cylindrical Implosion Experiments and Proton Radiography

In order to validate the compaction models developed in this work, validation data must be generated which accurately measures the shock response of a brittle, distended material under shock loading. At LANL, the Los Alamos Neutron Science Center's (LANSCE), shown in **Figure 3.7a**, Proton Radiography (pRad) facility, shown in **Figure 3.7b**, has been used to directly and accurately measure the real densities of materials during the shock loading process. These direct density measurements have a spatial resolution of approximately  $60\text{ }\mu\text{m}$  with a field-of-view of  $37\text{ mm}$ , and a temporal resolution of up to  $200\text{ ns}$  per frame for up to 31 frames. Examples of proton radiographs produced at pRad are shown in **Figures 3.7c** and **3.7d**, where measured density is shown as a spectrogram displaying higher densities in red and lower densities in blue [42, 43].

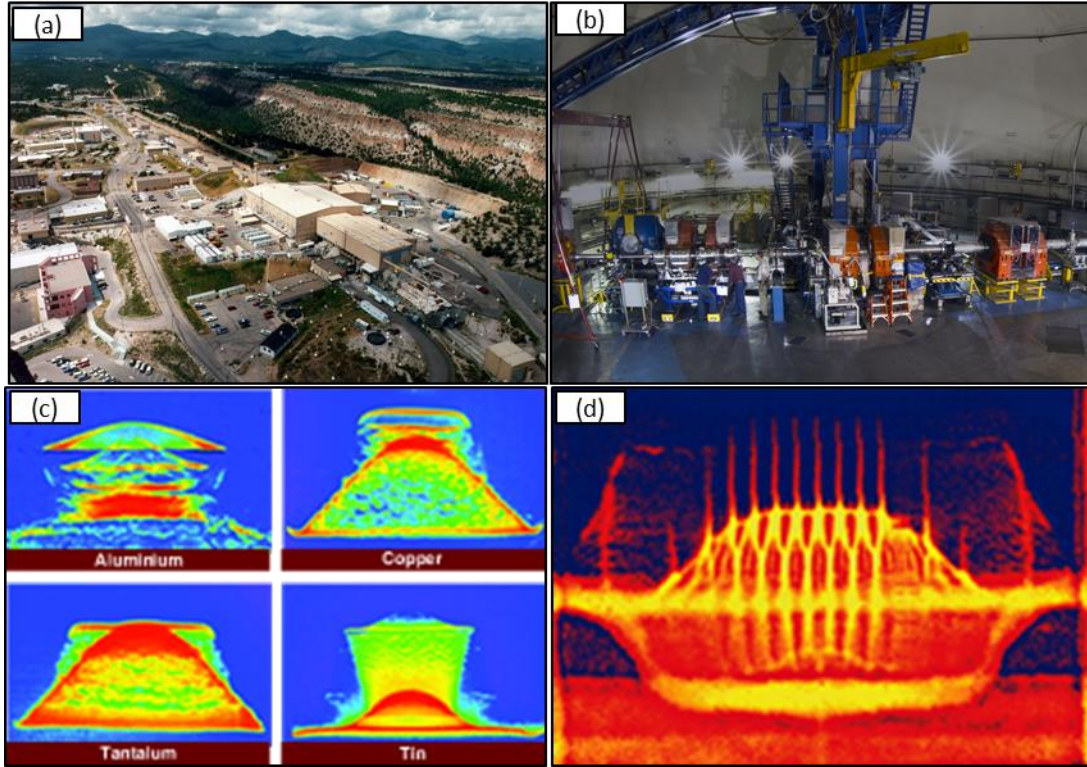


**Figure 3.7.** Overview images of proton radiography at LANL showing (a) sky-view of LANSCE linear accelerator, (b) beam line and magnetic lenses in pRad experimental area, (c) example spectrogram of in situ density measurements during a spall experiments, and (d) example spectrogram of in situ density measurements during a Richtmyer-Meshkov instability experiment [42].

The proton beam used at the pRad facility to image and measure materials under shock loading is a cylindrically focused beam with a Gaussian distribution of proton flux. This makes cylindrical geometries ideal for experimental work with pRad. Of primary interest in this work will be the Precision High Energy-density Liner Implosion eXperiment (PHELIX).

PHELIX at LANL is a pulsed power liner implosion machine. It uses a capacitor bank and toroidal capacitor, shown in **Figure 3.8a**, to electromagnetically drive high energy-density implosions [44]. PHELIX is wholly housed in a shipping container, making the machine mobile. A simplified view of the PHELIX implosion mechanism is shown in **Figure 3.8b**, and an example x-ray radiograph of an experiment fielded on PHELIX is shown in **Figure 3.8c**, showing a longitudinal projection view of an imploding liner moving inwards toward a 3D printed PDV probe holder [45]. Being a mobile

machine, PHELIX is able to be moved into the LANSCE beamline to be imaged via pRad during a dynamic experiment. As such, model validation experiments will be conducted utilizing pRad to image the implosion behavior of a cylindrical ceria powder compact fielded on PHELIX. In order to determine the ideal test geometries for this validation experiment, preliminary modeling work will be performed using the LANL hydrocode FLAG. In these computations, ceria will be modeled using two basic compaction models calibrated using preliminary experimental data gathered from plate impact experiments conducted at LANL and Georgia Tech.

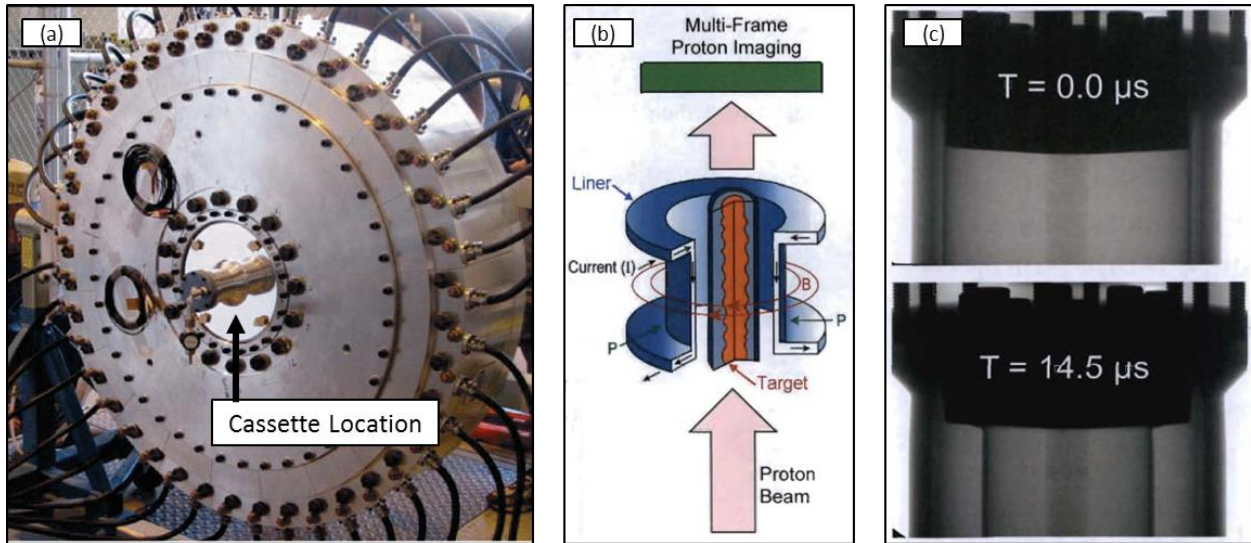


**Figure 3.8.** Overview of PHELIX showing (a) the PHELIX transformer and cassette location (b) diagram of PHELIX implosion process, and (c) longitudinal x-ray radiograph of liner implosion process during a test shot [44].

### 3.6. Computational Modeling Using LANL Hydrocode FLAG

FLAG is a multiphysics hydrocode developed by LANL. It is primarily Lagrangian-based; however, it incorporates Arbitrary Lagrange-Eulerian (ALE) capabilities and may be run in an entirely Eulerian format. FLAG is characterized by its use of unstructured meshes and a staggered grid code [46]. In the proposed work, FLAG is used as a computational tool to investigate the ability of existing compaction models to both describe and predict the dynamic compaction behavior of ceria powder

compacts under uniaxial shock loading via gas gun impact and cylindrically converging shock loading via pulsed power liner implosion.

FLAG is outfitted with a variety of compaction models with varying levels of complexity, including three forms of the P-alpha compaction model: PACXP (Modified Boade, 2 term exponential form), PaMenKo (Menikoff-Kober), and PaPPL (perfectly plastic approximation) [47]. In this study, all forms of the P-alpha compaction model which have existing FLAG nodes will be investigated for their prediction capabilities. Additionally, a first-approximation FLAG node referred to as the Ramp model will be investigated as a baseline. The Ramp model is not thermodynamically consistent and directly calculates pressure as a function only dependent on density [47, 25]. A comparison of the PACXP and Ramp models used in the FLAG hydrocode are shown in **Figure 3.9**.

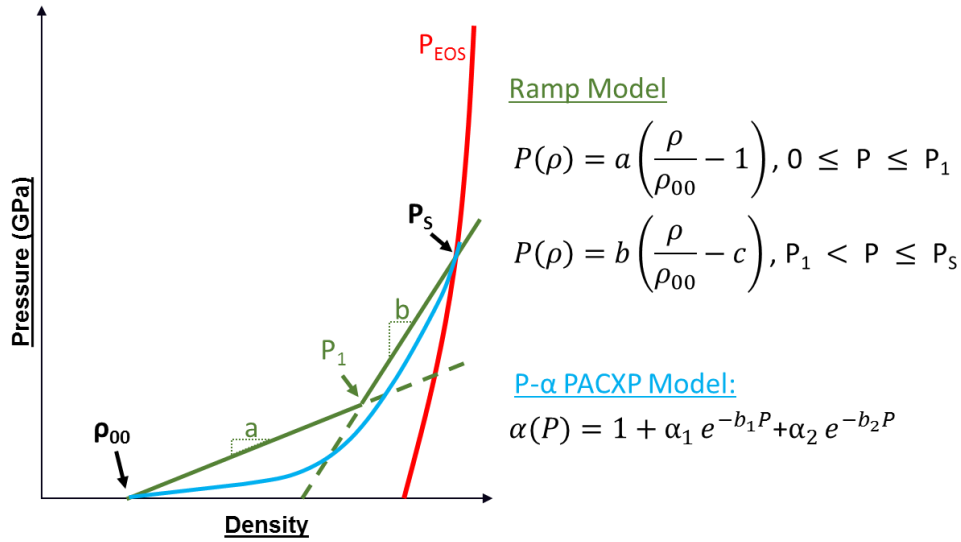


**Figure 3.9.** Comparison of PACXP and Ramp compaction models used in FLAG.

The computational work will be done by first fitting the compaction model functional forms to the gas gun impact data produced for ceria compacts at Georgia Tech and LANL. The fitted compaction models will then be used to run simulations of the completed experiments with equivalent geometries and impact conditions. The output computational data will then be compared to the experimentally measured particle velocity profiles of the ceria-window interface.

The best fit 1D compaction models will then be used to determine the ideal experimental geometries for a 2D experiment fielded on PHELIX at pRad, with the goals of the experiment being (1) to produce the most cylindrically planar shock into the ceria powder possible, (2) to create a distinct gradient of density in the powder compact without reaching full density, and (3) to conduct the experiment with no leak of powder out of the experimental capsule. The experimental parameters which yield the best possible density profile in the simulated material for a majority of simulated compaction models, while also ensuring that no powder escapes the experimental chamber during or after the experiment, will be implemented as the experimental parameters for the first group of validation experiments. After the first group of validation experiments is completed and their experimental data fully processed and analyzed, subsequent PHELIX validation experiment parameters will be optimized using only the compaction model which best fits the initial validation experiment data.

## CHAPTER 4

### PRELIMINARY RESULTS AND DISCUSSION

Based on the objectives of the proposed work, a series of preliminary experiments were performed to gather compaction data for ceria powders. An initial series of simulations was also performed to correlate model predictions with measured data as well as to design 2D compaction experiment geometries. In this chapter, the preliminary data gathered from the first three plate impact experiments performed are shown and discussed. Computational modeling efforts focused on describing these plate impact experiments and determining ideal test geometries for the PHELIX compaction experiment performed at LANL are also presented. The chapter finishes with a discussion of preliminary data from the first two PHELIX compaction experiments, highlighting discrepancies between experimental and computational data that will be the focus of future modeling work.

#### 4.1. Preliminary Gas Gun Plate-Impact Compaction Experiments

A set of three plate impact compaction experiments on ceria powders have been performed at Georgia Tech to assist with validating the newly developed experimental design presented in the previous chapter. The first validation experiment was to reproduce shock Hugoniot data previously gathered at LANL [9, 8], based on plate impact experiments performed on 4.05 g/cc (56.1% TMD) rods morphology ceria powder compact at 405 m/s.

The plate impact experiment at Georgia Tech was performed on similar rods morphology ceria powder, a 4.04 g/cc (56.0% TMD) rods morphology ceria powder compact at 387 m/s, experiment #1701. The extracted shock Hugoniot data for the Georgia Tech experiment #1701 overlaps well with the LANL experiment #56-11-27, as shown in **Table 4.1**. The velocity profiles for both experiments are plotted in **Figure 4.1**.

**Table 4.1.** Comparison of shock Hugoniot data collected at LANL to preliminary data collected at Georgia Tech.

| Facility     | Shot ID  | $\rho_{00}$ (g/cc) | $V_{imp}$ (km/s)     | $U_s$ (km/s)       | $u_p$ (km/s)        | P (GPa)            | $\rho$ (g/cc)      |
|--------------|----------|--------------------|----------------------|--------------------|---------------------|--------------------|--------------------|
| LANL [9, 8]  | 56-11-27 | 4.05<br>(0.18)     | 0.405<br>$\pm 0.001$ | 1.23<br>$\pm 0.01$ | 0.355<br>$\pm 0.01$ | 1.78<br>$\pm 0.08$ | 5.69<br>$\pm 0.15$ |
| Georgia Tech | 1701     | 4.04<br>(0.16)     | 0.387<br>$\pm 0.001$ | 1.26<br>$\pm 0.02$ | 0.339<br>$\pm 0.01$ | 1.73<br>$\pm 0.06$ | 5.53<br>$\pm 0.06$ |

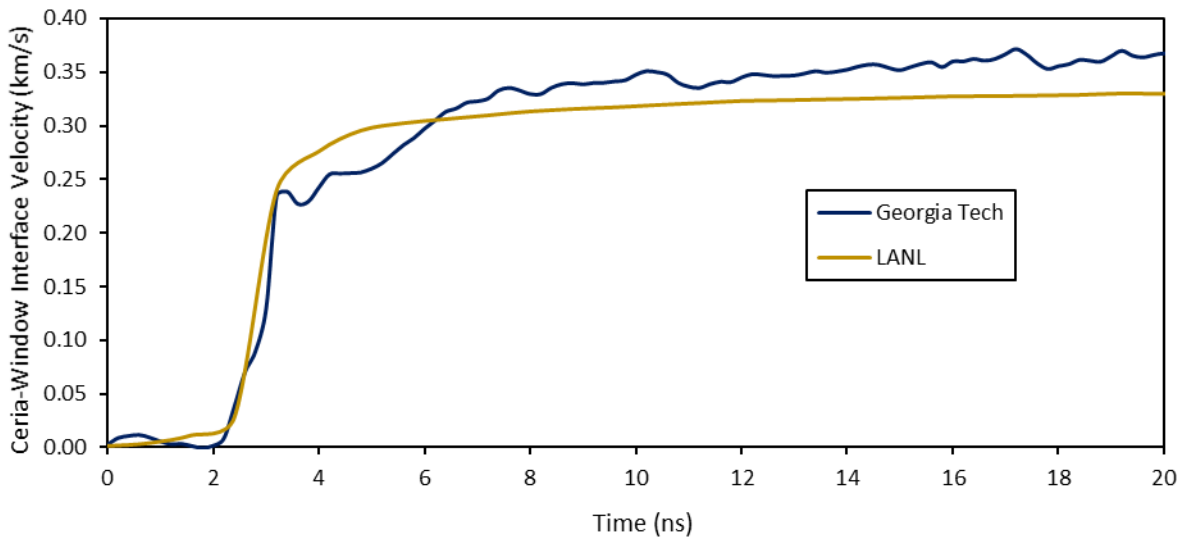


**Figure 4.1.** Comparison of VISAR-recorded powder-window interface velocities measured at LANL and Georgia Tech. Slight variations are seen between the two data sets, but overall trends are mostly similar.

With the newly designed and tested experimental procedure validated against LANL experimental data, the second shock compaction experiment at Georgia Tech was focused on measuring the shock response of the equiaxed ceria powder with a higher green density that had not been tested before: 4.5 g/cc (62.5% TMD). The experiment #1702 was performed under similar conditions to those used in experiment #1701, with the variations being ceria powder morphology (equiaxed) and higher powder compact green density. Experiment #1702 was thus performed on 4.51 g/cc (62.6% TMD) equiaxed morphology powder shock compact at 389 m/s.



The third plate impact experiment conducted at Georgia Tech aimed to investigate the behavior of the 62.5% TMD equiaxed ceria powder compact at a lower impact velocity. As such, experiment #1703 was performed on the 4.47 g/cc (62.0 % TMD) equiaxed morphology powder compact at 251 m/s. The data collected from each of the three experiments performed at Georgia Tech are shown in **Table 4.2**. In this table, the initial density ( $\rho_{00}$ ), impact velocity ( $V_{imp}$ ), and shock velocity ( $U_s$ ) are all measured parameters. The particle velocity ( $U_p$ ), pressure ( $P$ ), and shock compressed density ( $\rho$ ) are calculated using the measured parameters and the impedance matching technique. Uncertainties are quantified according the high fidelity Hugoniot analysis method proposed by Fredenburg [9].

**Table 4.2.** Tabulated shock Hugoniot data collected from the first three Georgia Tech plate impact experiments. Data are shown with quantified errors; errors in parenthesis represent the full spread of possible measured values, while symmetric errors represent uncertainties calculated via quadrature.

| Shot ID | Morphology | $\rho_{00}$ (g/cc) | $V_{imp}$ (km/s)     | $U_s$ (km/s)       | $u_p$ (km/s)         | $P$ (GPa)          | $\rho$ (g/cc)      |
|---------|------------|--------------------|----------------------|--------------------|----------------------|--------------------|--------------------|
| 1701    | Rods       | 4.04 (0.16)        | 0.387<br>$\pm 0.001$ | 1.26<br>$\pm 0.02$ | 0.339<br>$\pm 0.01$  | 1.73<br>$\pm 0.06$ | 5.53<br>$\pm 0.06$ |
| 1702    | Equiaxed   | 4.51 (0.08)        | 0.389<br>$\pm 0.001$ | 1.54<br>$\pm 0.01$ | 0.326<br>$\pm 0.001$ | 2.27<br>$\pm 0.04$ | 5.73<br>$\pm 0.06$ |
| 1703    | Equiaxed   | 4.47 (0.08)        | 0.251<br>$\pm 0.001$ | 1.48<br>$\pm 0.01$ | 0.212<br>$\pm 0.001$ | 1.40<br>$\pm 0.03$ | 5.22<br>$\pm 0.05$ |

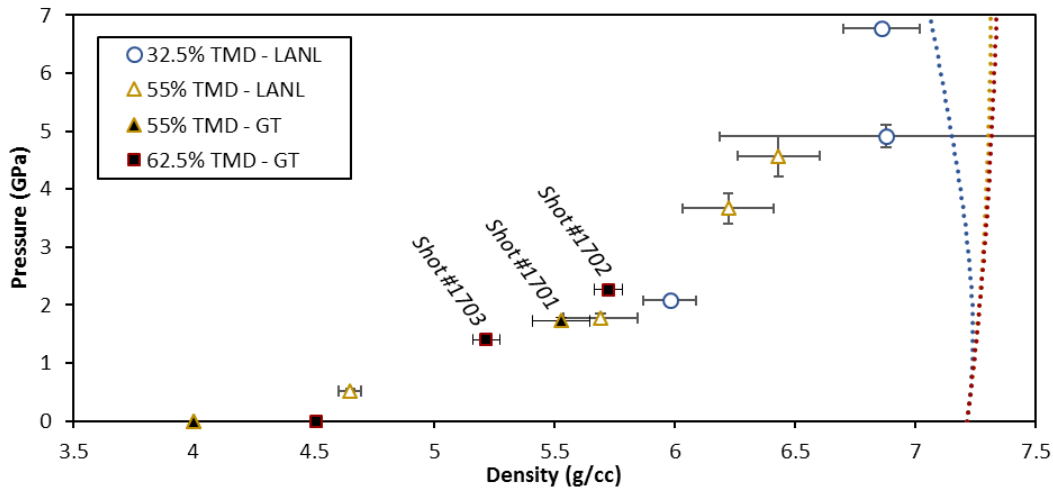


**Figure 4.2.** Plotted pressure-density shock Hugoniot data for ceria powders from the current study plotted in comparison to data collected in previous experiments at LANL [9, 40].



**Figure 4.2.** plots the pressure-density Hugoniot data for the first three Georgia Tech plate impact experiments along with data from experiments performed at LANL. The combined data reveal the possibility of an elastic region in the 62.5% TMD equiaxed ceria compacts that has not been validated in previous research. Data from the LANL experiments performed on ceria capsules at 32.5% and 55% TMD do not show an obvious trend with a well-defined elastic region. Due to this, the dynamic compaction behavior of both the 32.5% TMD and 55% TMD powder compacts may be modeled on the same compaction curve using the same compaction model, a generalized  $P$ - $\alpha$  formula that assumes a negligible elastic region. The preliminary results provide a motivation for further experiments at lower impact velocities and higher green densities to further validate the observed trend.

#### **4.2. Simulations of Georgia Tech Plate Impact Experiments**

Using the LANL multiphysics code FLAG, version 3.7.Alpha.4, simulations of the first three plate impact experiments conducted at Georgia Tech were completed using a variety of compaction models. The simulated geometry is 1D, with a single element dimension of 5  $\mu\text{m}$ . The model geometry is shown schematically in **Figure 4.3**. The compaction model parameters for ceria compacts with an initial density of 4.00 g/cc (55% TMD) were fit to experimental data collected at LANL [8, 9] and the one experiment conducted at Georgia Tech. Because only two shock compaction experiments have been performed on 62.5% TMD powder compacts, the 55% TMD model parameters were also used to simulate 62.5% TMD ceria compacts. Nevertheless, it was observed that the output computational tracer data at the powder-window interface closely resemble experimental VISAR data. An overlay of the experimental and computational particle velocity data, produced using the PACXP node, for 62.5% TMD compaction experiments at two different impact velocities is shown in **Figure 4.4**.

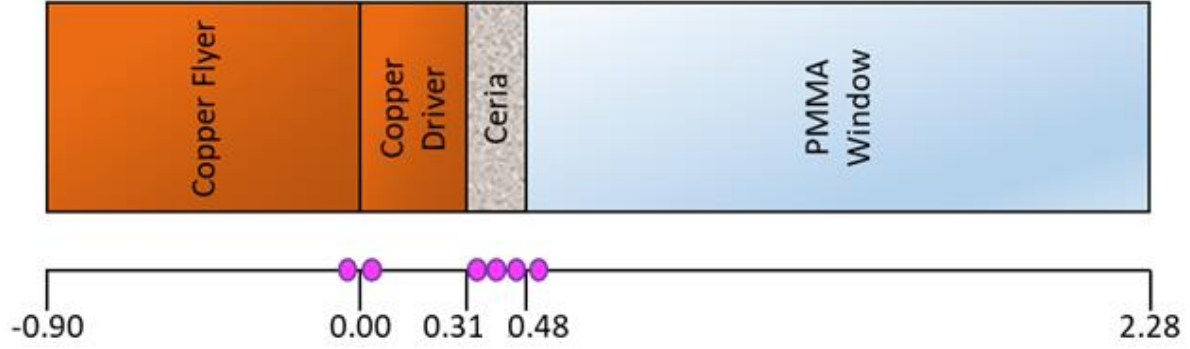


**Figure 4.3.** 1D geometry used in initial simulations of GT experiments. The six tracer locations are shown qualitatively as points on the x-axis with values in cm.

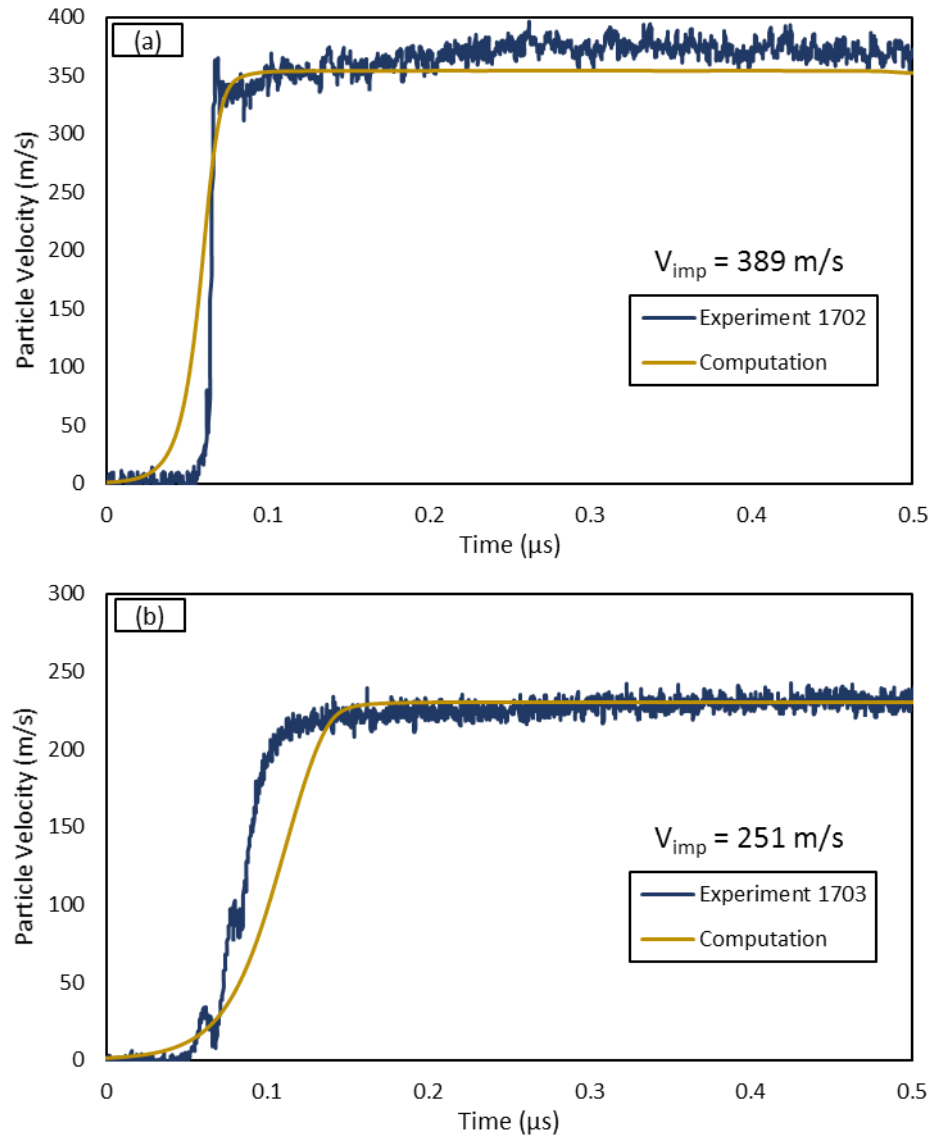


**Figure 4.4.** Comparisons of computational (PACXP) and experimental data for 62.5% TMD ceria powder compacts impacted at (a) 389 m/s, and (b) 251 m/s.

In general, there is good agreement in the maximum steady state particle velocities for the first experiments on ceria powder 1D FLAG computations, although the rise times do not match with the experimental data. Further work is ongoing to adjust parameters such as the artificial viscosity, etc. and obtain correlation.

### 4.3. PHELIX Compaction Experiments: Simulations and Preliminary Data

Initial simulations of the PHELIX validation experiments (described in the previous chapter) began as 1D computations with constant velocity liner impacts. These simulations were focused on determining the ideal thicknesses of the aluminum cylinder (containing the ceria compact) and the aluminum liner. Subsequent simulations incorporated magnetohydrodynamic (MHD) drive conditions to simulate the acceleration of the liner to impact. 1D geometry determination was focused on assessing the geometry and drive conditions that would produce density profile plots in which the input shock wave is steady for the longest period without fully compacting the powder. The 1D geometry used in these computations is shown in **Figure 4.5** and an example of the output data is shown in **Figure 4.6**.

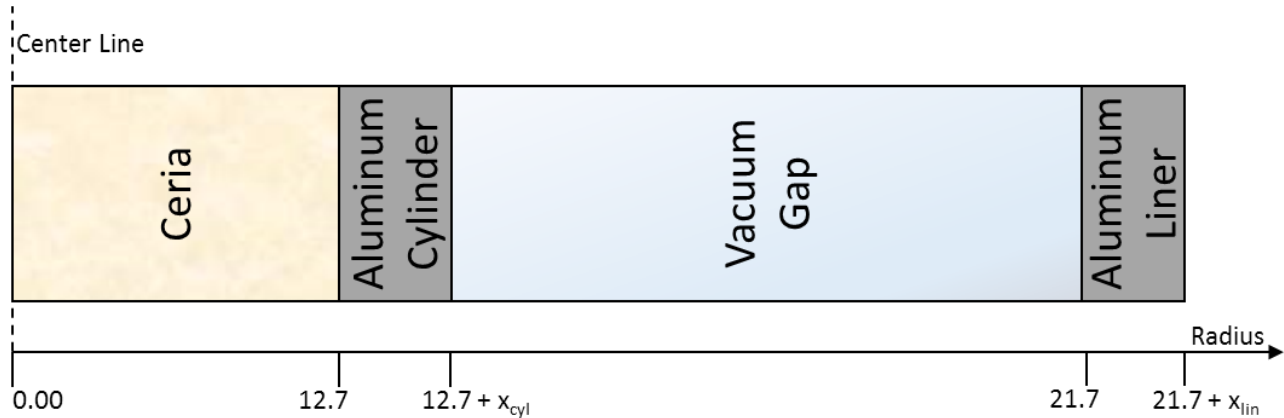


**Figure 4.5.** Example 1D simulated geometry used in initial modeling of PHELIX. Because PHELIX is symmetric about the Z-axis, simulated geometries are modeled from the center point outwards. Plotted values reflect radial distances from the center of the ceria cassette with units in mm. The variables  $x_{cyl}$  and  $x_{lin}$  refer to the thickness of the cylinder and the liner, respectively.

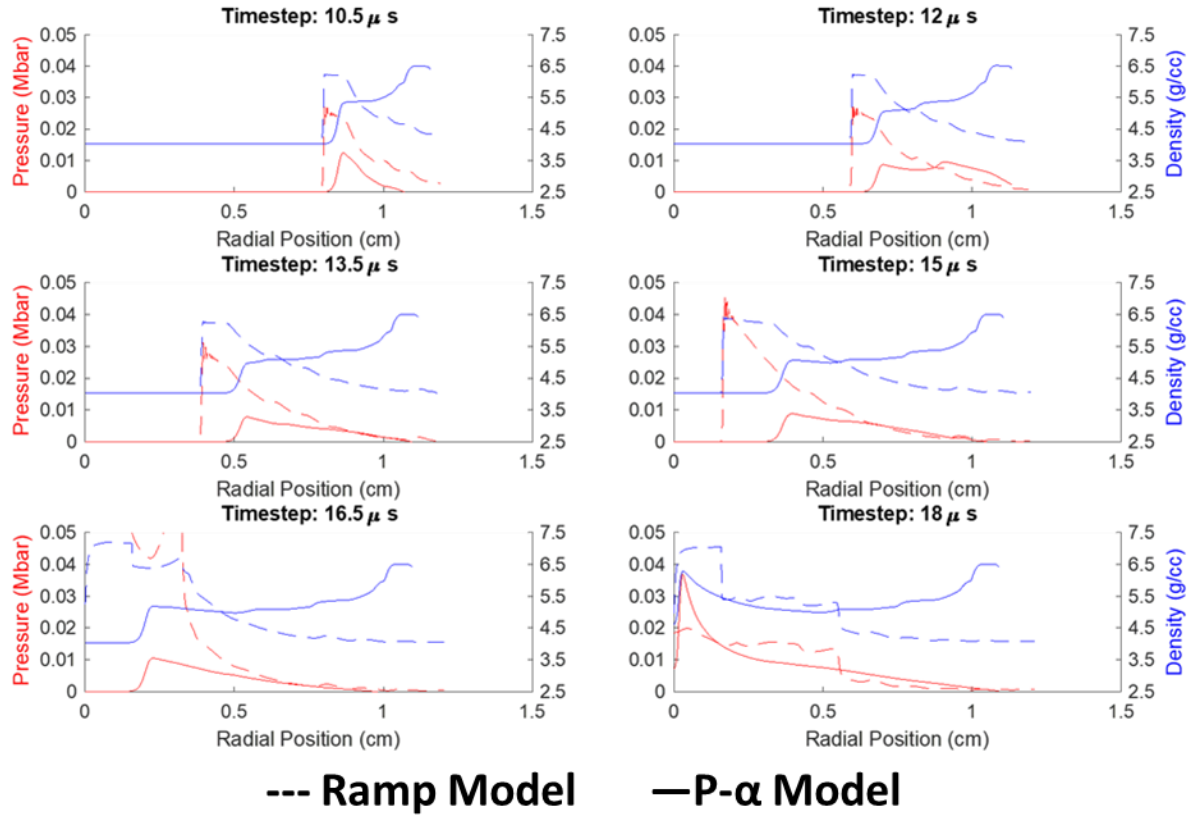


**Figure 4.6.** Examples of pressure (red) vs. radial position vs. density (blue) plots, at six time steps, for computed variables of 1 km/s impact velocity, 2.5 mm cylinder wall, 1.25 mm liner, using either the P- $\alpha$  PACXP (solid line) or Bi-linear Ramp (dashed line) compaction models available in FLAG.

From these initial simulations, four possible geometry variations were selected and studied with a 2D geometry: cylinder wall thicknesses of 2.0 and 2.5 mm and liner thicknesses of 1.00 and 1.25 mm.

2D computations evaluated both the P- $\alpha$  PACXP and Bi-linear Ramp compaction models (model forms discussed in previous chapter) while varying the angle and curvature of the PHELIX glide plane, the material and thickness of ceria cassette end caps, and the PHELIX capacitor charge. An example of a 2D simulated PHELIX implosion using a 90 kV charge is shown in **Figure 4.7** as a longitudinal cross section. These output data are plotted as spectrograms of velocity, density, kinetic energy, and pressure at six time steps, with zero time indicating the beginning of current flow.

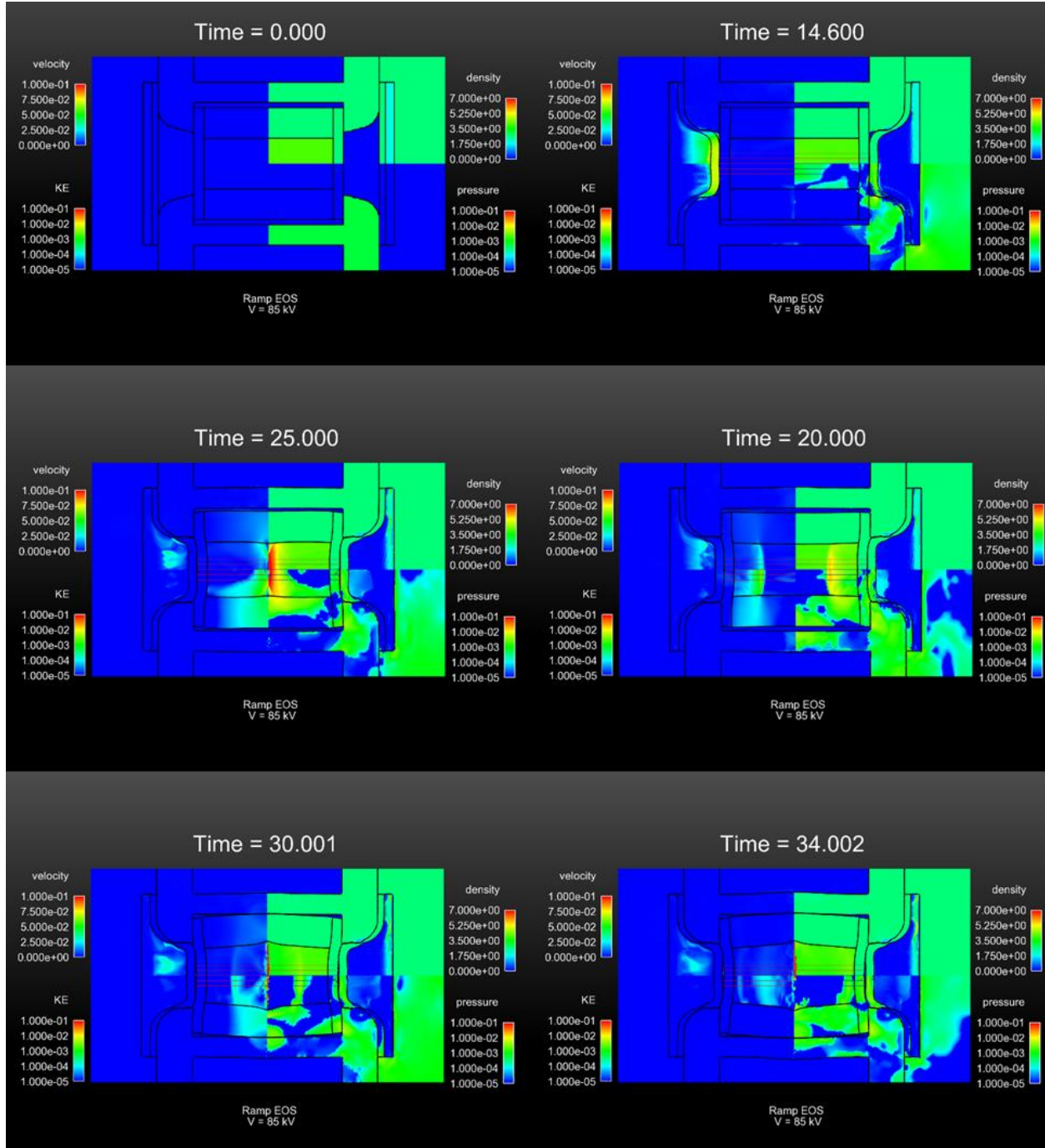


**Figure 4.7.** Example of 2D simulation of PHELIX. This simulation uses a 2.0 mm cylinder, 1.25 mm flyer, and 90 kV capacitor charge and the Bi-linear Ramp compaction model. The output data is shown with spectrogram maps of velocity, density, kinetic energy, and pressure.

Immediately prior to performing the first PHELIX compaction experiment, computed tomography scans of a pressed ceria PHELIX cassette were taken using the 6 MeV Microtron at the LANL

LANSCE facility. Sample tomographic images are shown in **Figure 4.8**, exhibiting minimal density gradients within the powder compact. Following tomography, the first PHELIX experiment was conducted using the 2D geometries computationally evaluated via FLAG, which produced the safest possible response, i.e., no leak of powder outside the cassette and no fracture or spall damage to the powder cassette. Montage proton radiography images collected at the LANL pRad facility are shown in **Figures 4.9** and **4.10** for these first two validation experiments. While the exact density data from these images is still being processed, initial first order approximations show significant discrepancies in the experimental and computational data near the center of the imploding powder cassette. The computational data predicts the center of the powder cassette to be the highest density found in the material and the experimental data shows the lowest density values found at the center of the ceria cassette. This discrepancy is likely due to a miscalculated attenuation variable, possibly stemming from microstructural parameters.

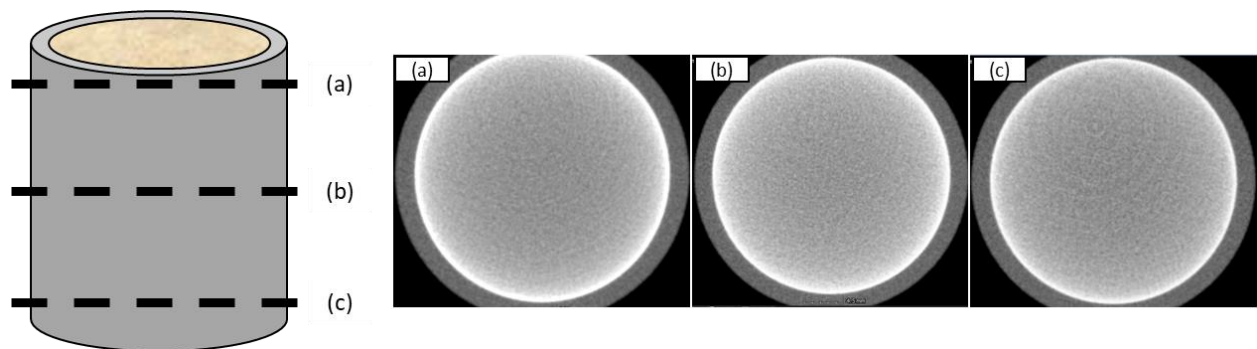


**Figure 4.8.** Computed tomographic images of a pressed ceria PHELIX cassette taken using the 6 MeV LANL Microtron. The transverse cross sections shown are representative of the (a) top, (b) middle, and (c) bottom of the powder cassette. A bright ring is seen at the powder-cylinder interface due to anomalous scattering.

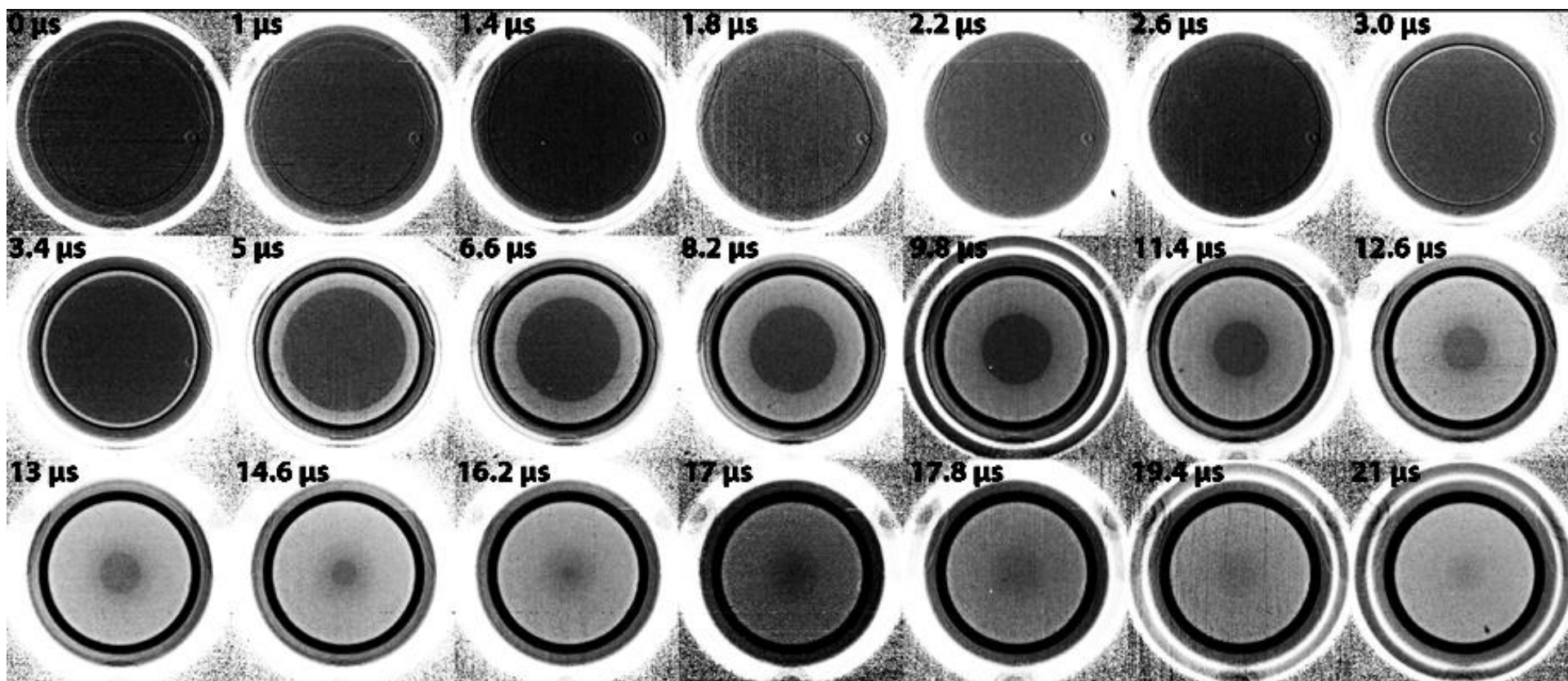


**Figure 4.9.** Montage of proton radiographs taken during the first PHELIX compaction experiment. This experiment was performed using an 85 kV capacitor charge and images were taken using seven 3-frame cameras. Data is shown as an inverse transmission plot, such that higher density is shown as a lighter shade. Timing is relative to LANSCE beamline.



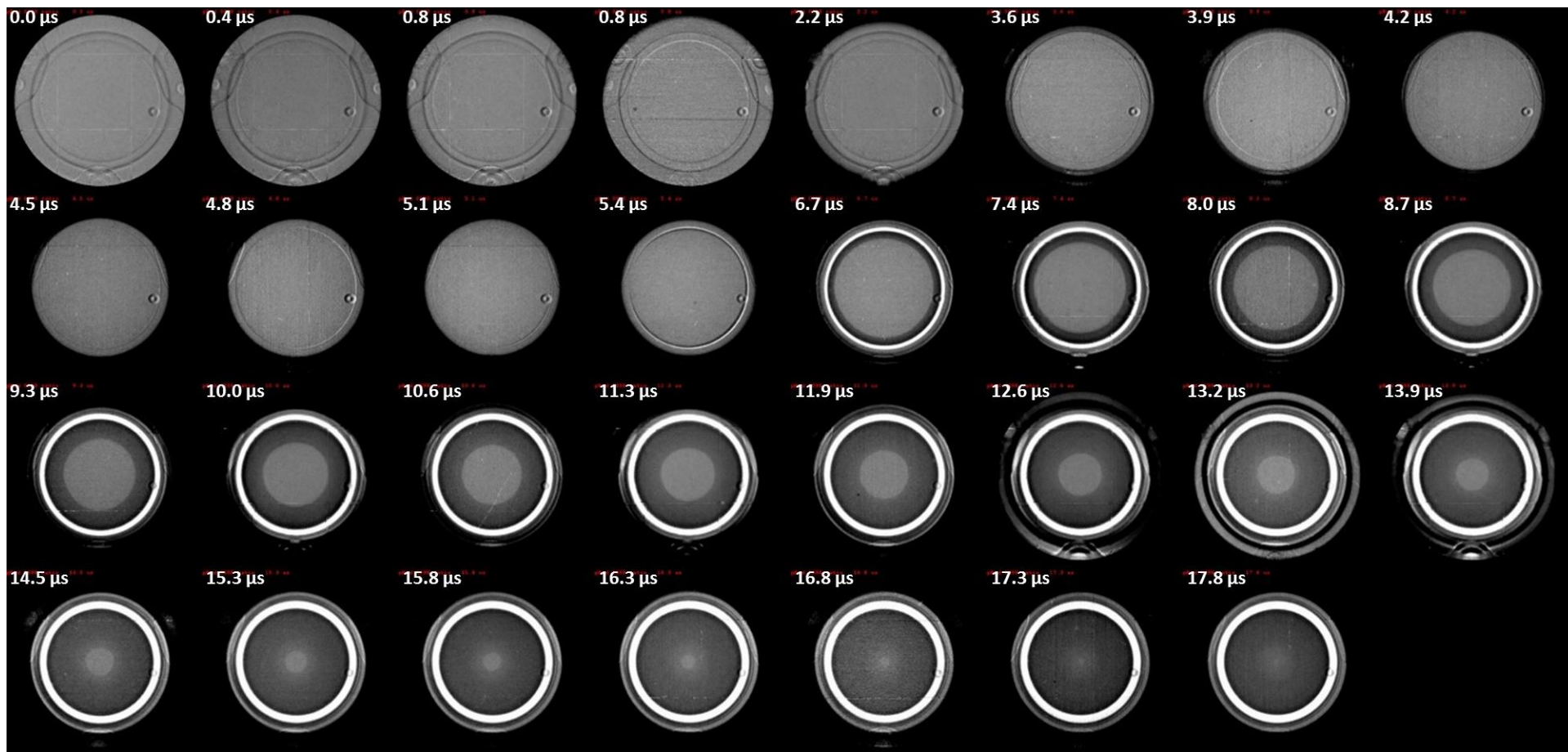


**Figure 4.10.** Montage of proton radiographs taken during the second PHELIX compaction experiment. This experiment used a 90 kV capacitor charge and images were taken using seven 3-frame cameras and one 10-frame camera. Data is shown as transmission plots, such that higher density is shown as a darker shade. Timing is relative to LANSCE beamline.



## CHAPTER 5

### PROPOSED FUTURE WORK

Initial research efforts have produced compaction data obtained from three gas gun plate impact experiments and two liner implosion compaction experiments. Additional high-fidelity, high-precision data is needed to produce a predictive model. Future work will largely focus on gathering the additional high-precision dynamic compaction data for two morphologies of ceria powders and varying initial densities. With appropriate additional experimental compaction data, work will pivot to a theoretical focus. Theoretical research efforts will focus on first augmenting existing compaction models to better predict the shock compaction response of brittle ceria powders, then on predicting the response of brittle powders in general.

#### 5.1. Plate Impact Experiments: Density and Particle Morphology Variations

Immediate future work will focus on conducting uniaxial strain plate-impact dynamic compaction experiments for ceria powder compacts. The focus of these experiments will be to precisely characterize powder compact behavior as a function of green density and particle morphology.

From the preliminary data collected for the first two 62.5% TMD ceria compaction experiments, a possible elastic compaction regime may have been observed. This differs from previously observed compaction trends for powder compacts of lower green densities, which have negligible elastic regions. This possible elastic response was pronounced at low pressures and high green densities. In order to investigate the physical mechanisms that may cause this behavior, future work will first focus on low velocity impacts, between 150 and 400 m/s, with high density powder capsules, 62.5% TMD and 70% TMD. **Table 5.1.** lists the proposed experimental conditions intended

for future experiments. The experimental conditions may change in order to probe specific pressure and density regions.

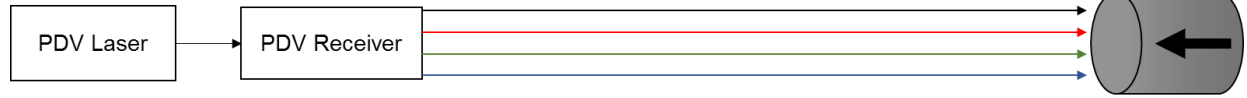
**Table 5.1.** Proposed experimental conditions for future plate impact experiments.

| Morphology | %TMD | $\rho$ (g/cc) | Impact Velocity (km/s) |     |     |     |     |      |
|------------|------|---------------|------------------------|-----|-----|-----|-----|------|
| Equiaxed   | 44.0 | 3.17          | 150                    | 250 | 400 | 600 | 800 | 1000 |
| Equiaxed   | 62.5 | 4.51          | 150                    | X   | X   | 600 | 800 | 1000 |
| Rods       | 44.0 | 3.17          | 150                    | 250 | 400 | X   | 800 | X    |
| Blend      | 70.0 | 5.05          | 150                    | X   | 400 | X   | 800 | X    |

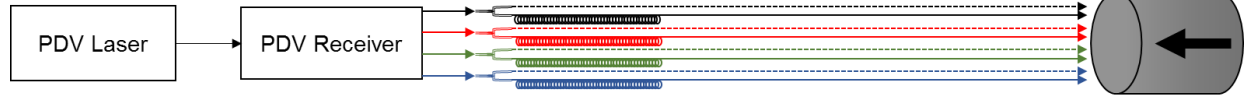
## 5.2. Improved Velocity Interferometry Diagnostics: PDV Multiplexing

Currently, the use of a 4-channel PDV allows accurate measurements of a maximum of two transit wave velocities through the thickness of the powder compact. Use of additional measurements can help to further characterize and understand variations in the wave velocity across different regions of a powder compact. One method that can increase the measurement capabilities of a PDV is multiplexing, which allows multiple signals to be measured on a single receiver. For a PDV system, this is done by splitting the output laser light into separate fibers of varying lengths. Different length fibers create varying optical delays for reflected laser light. The difference in these optical delays causes simultaneously occurring signals to be displayed at different step times on the same channel. A diagram of two levels of multiplexing is shown in **Figure 5.1.** and an example of time shifted data obtained from a preliminary experiment is shown in **Figure 5.2.**

Base Level PDV System: 4 Probes



Multiplexed One Level: 8 Probes



Multiplexed Two Levels: 12 Probes



**Figure 5.1.** Diagram showing the possibilities of multiplexing, with separate laser channels color coded and multiplexed lines within a channel coded by line pattern. Spirals along a fiber indicate a sufficiently long amount of fiber to create an optical delay.

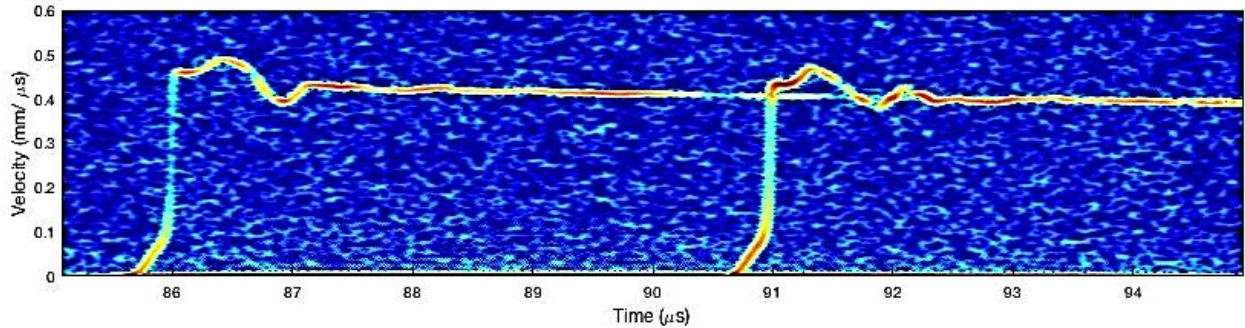


**Figure 5.2.** Spectrogram of multiplexed PDV data. These data were collected from the free surface velocity of a steel-steel symmetric impact. The optical delay in these data was created using 1 km of bare fiber and is approximately 4.9 μs.

Multiplexing multiplies the number of usable velocity probes in a PDV system by each level of multiplexing implemented. The only limit to this increase of usable probes is the power of the input laser. The single level multiplexed data shown in **Figure 5.2** was collected using 25% of the PDV laser's maximum power output. This demonstrates the possibility of increasing the PDV system to seven to nine levels of multiplexing (8-10 probes per channel), allowing 32-40 separate PDV probe measurements on four PDV channels. With this many PDV measurements available, spatially resolved velocity measurements are possible, allowing for more accurate measurements of shock and particle velocity as well as determining the meso-scale effects of the heterogeneous structure of the powder compacts.

### 5.3. Spatially Resolved PDV Measurements

Spatially resolved measurements employing the line VISAR and line ORVIS (Optically Reflected Velocity Interferometer System) are optical velocimetry methods that utilize interference fringes, collapsed into a line geometry, to measure velocity across the back of a sample. Line VISAR and line ORVIS are cumbersome to set up, sometimes taking days to weeks to align for a single shot. Additionally, these measurements output streak images, which are difficult to process in a consistent manner. This makes the development of a simpler spatially resolved diagnostic capability highly favorable. The proposed method in this research is to employ a line PDV.

Similar to the line VISAR and line ORVIS, the line PDV would take velocity measurements across a defined distance on the back of a sample. However, while line VISAR and line ORVIS use optics to shape a single laser light into a 1D geometry, line PDV splits the output laser light to a large number of separate probes, which each measure velocity separately. The advantage of line PDV is its modular nature and quick set up. The modular nature of line PDV introduces a key data collection safety feature of redundancy. This safeguard alone makes line PDV extremely resilient to failures such as faulty probes, e.g., a 32-probe line PDV can allow up to 31 probe failures in a single experiment and still successfully collect usable data. In comparison, if line ORVIS or line VISAR have a probe failure, all data is lost. The modular nature of Line PDV also allows the measurement of particle velocities along various length scales and shapes, as the probes used in line PDV may be aligned as far apart as needed, or as close together at the thickness of a bare single mode fiber optic (125  $\mu\text{m}$ ). Line PDV is also much easier to set up than line VISAR and line ORVIS. This is because PDV probes produce clearer signals when not perfectly aligned, making their set-up time on the order of seconds to minutes.

In the present work, line PDV measurements will be conducted using a line of multiplexed PDV probes with measured positions. The hope is to conduct a significant amount of multiplexing

on the PDV system to gain the capability of fielding at least 16 PDV probes in a line across the back of a sample. A diagram of a line PDV concept employing 40 PDV probes across a 1.75 inch line is shown in **Figure 5.3**.

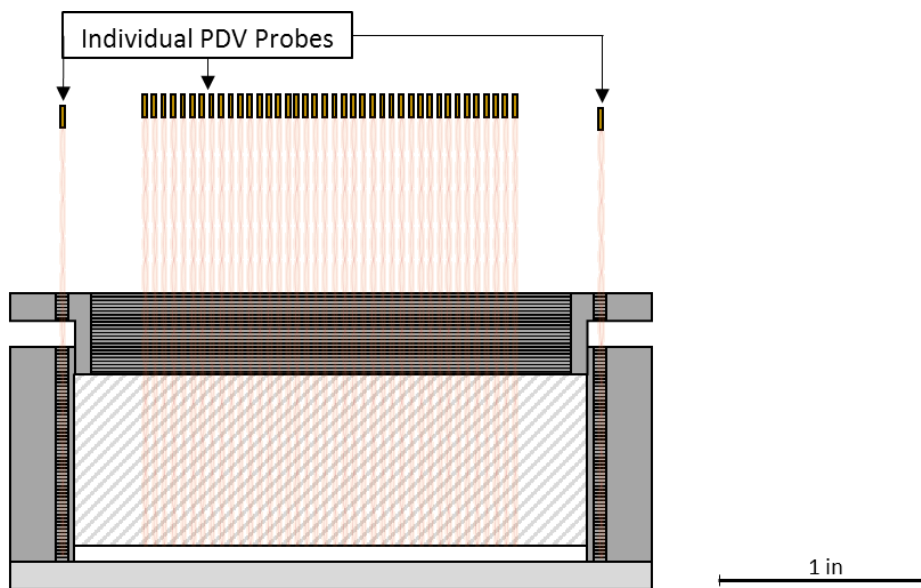


**Figure 5.3.** Line PDV concept drawing, showing how a 38-probe line PDV may be fielded across 1.75 inches of the powder-window interface in the low density powder capsule during a plate impact experiment.

#### 5.4. Modeling Parametrization and Development

Modeling work will continue in concert with experiments. As more high-precision shock compaction data is collected for ceria, better trends in material behavior will be established to guide model development. Future continuum modeling work will first focus on improving FLAG node parameters to better model the PHELIX compaction experiments using the compaction models available in FLAG. Although no model currently captures the shock attenuation affect seen in the PHELIX compaction experiments, present theoretical work at LANL using the Menikoff-Kober  $P-\alpha$  model is showing the highest convergence of any model for plate impact data.

## **5.5. Additional PHELIX Compaction Experiments**

Future work with PHELIX will be focused on processing the data collected from the first two PHELIX compaction experiments. These experiments are extremely data-rich, directly measuring wave position, material density, and wave pulse shape information with high spatial and temporal resolution. The extracted data from these experiments will be helpful in determining both model validity and the applicability of the impedance matching technique for powders.

Future PHELIX experiments will focus on characterizing the effects of powder particle morphology and green density on the dynamic compaction behavior of ceria. The pRad data collected from future experiments on rods powder ceria will help to determine the exact effects of particle morphology on shock compaction behavior, as both shock velocity and shocked density are directly measured using this technique.

### **5.5.1 PHELIX Validation of Impedance Matching Technique for Powders**

The impedance matching technique has been commonly employed to determine the shocked state of powders. However, this method requires that the propagating shock wave be perfectly discontinuous and the shocked material be inviscid, invalidating its use for powders. As such, calculating the shocked state of a powder via impedance matching is inherently flawed; however, no researchers have investigated the magnitude of this flaw in the dynamic compaction of brittle powders.

Future proposed work will investigate the validity of the impedance matching technique to determine the shocked density of a brittle powder through analysis of the proton radiography images taken during the PHELIX compaction experiment. These images directly measure the shock compressed density of the powder compact, as well as shock velocity, impact velocity, and initial

density. Using these data, the shocked density of the powder compact calculated via impedance matching may be validated against the shocked density directly measured via proton radiography.

## **5.6. Expected Outcome and Potential Challenges**

The proposed research will produce high-fidelity, high-precision data for the shock compaction response of ceria powder as a function of powder compact green density and particle morphology, thus revealing any microstructural dependencies on material behavior. Compaction models will be calibrated to this data, creating a predictive compaction model for ceria powders that incorporates microstructure. Because the physical compaction mechanisms in brittle powders are dominated by the processes of fracture and consolidation, which create and reduce free surface area in a compact, it is hypothesized that a compaction model for brittle materials will need to incorporate some aspect of surface energy in the total energy balance.

One potential challenge that may be faced during model development is trying to predict the behavior of the ceria cassette in the PHELIX experiment using compaction models calibrated to plate impact data. Compaction models are typically developed as a method to connect porous material physics to the solid equations of state. The shock waves induced by the PHELIX experiment are mostly unsteady while propagating into the ceria cassette. Unsteady waves move material responses off the normal Hugoniot equation of state response. Because of this, the developed compaction models will be attempting to predict material response beyond their calibration range. As such, parameterizing a compaction model that will model this behavior and do well in the off-Hugoniot response will be difficult.

## 5.7. Timeline

| Task                             | 2018   |        |      | 2019   |        |      |
|----------------------------------|--------|--------|------|--------|--------|------|
|                                  | Spring | Summer | Fall | Spring | Summer | Fall |
| Multiplexing                     |        |        |      |        |        |      |
| Plate Impact Experiments         |        |        |      |        |        |      |
| PHELIX Compaction 2              |        |        |      |        |        |      |
| Model Selection                  |        |        |      |        |        |      |
| Los Alamos Internships           |        |        |      |        |        |      |
| Model Development                |        |        |      |        |        |      |
| Correlate Model with Experiments |        |        |      |        |        |      |
| Thesis Writing                   |        |        |      |        |        |      |
| Completion of Degree             |        |        |      |        |        |      |



## REFERENCES

- [1] J. Forbes, *Shock Wave Compression of Condensed Matter: A Primer*, Springer-Verlag Berlin Heidelberg, 2012.
- [2] M. Meyers, *Dynamic Behavior of Materials*, John Wiley and Sons, 1994.
- [3] S. Holguin, *Physical Mechanisms of Laser-Activated Nanoparticles for Intracellular Drug Delivery*, Georgia Institute of Technology, 2017.
- [4] R. Serber, "The Los Alamos Primer," University of California, Los Alamos Scientific Laboratory, 1943.
- [5] P. Wesseling, *Principles of Computational Fluid Dynamics*, Springer Science & Business Media, 2009.
- [6] D. Fredenburg and et al, "Influence of the Initial Density on the Shock Compaction of CeO<sub>2</sub>," in *Shock Compression of Condensed Matter - AIP Conference Proceedings*, 2015.
- [7] D. Fredenburg and D. Dennis-Koller, "Interpreting the Shock Response of Porous Oxide Systems," in *Shock Compression of Condensed Matter - AIP Conference Proceedings*, 2013.
- [8] D. Fredenburg and et al, "The Influence of Morphology on the Low - and High-Strain-Rate Compaction Response of CeO<sub>2</sub> Powders," *Journal of Applied Physics*, vol. 115, no. 123511, 2014.
- [9] D. Fredenburg and et al, "High Fidelity Hugoniot Analysis of Porous Materials," *Review of Scientific Instruments*, vol. 84, no. 013903, 2013.
- [10] J. LaJeunesse and et al, "Dynamic Response of Dry and Water-saturated Sand Systems," *Journal of Applied Physics*, vol. 122, no. 015901, 2017.
- [11] V. Nesterenko, *Dynamics of Heterogeneous Materials*, Springer, 2001.
- [12] G. Crabtree, "From Quanta to the Continuum: Opportunities for Mesoscale Science," Basic Energy Science Advisory Committee (BESAC), 2012.
- [13] University of California, Los Alamos Scientific Laboratory, *LASL Shock Hugoniot Data*, S. Marsh, Ed., 1980.
- [14] e. a. R. McQueen, "The Equation of State of Solids from Shock Wave Studies," in *High Velocity Impact Phenomena*, New York Academic Press, 1970.

- [15] R. Boade, "Principal Hugoniot, Second-Shock Hugoniot, and Release Behavior of Pressed Copper Powder," *Journal of Applied Physics*, vol. 41, no. 4542, 1970.
- [16] F. Bauer, "Behavior of Ferroelectric Ceramics and PVF2 Polymers Under Shock Loading," in *AIP Conference Proceedings*, 1982.
- [17] e. a. Z. Duan, "Foil-like Manganin Gauges for Dynamic High Pressure Measurements," *Measurement Science and Technology*, vol. 22, no. 7, 2011.
- [18] D. Eakins and N. Thadhani, "Discrete Particle Simulation of Shock Wave Propagation in a Binary Ni+Al Powder Mixture," *Journal of Applied Physics*, vol. 101, no. 043508, 2007.
- [19] L. Barker and R. Hollenbach, "Shock-Wave Studies of PMMA, Fused Silica, and Sapphire," *Journal of Applied Physics*, vol. 41, no. 4208, 1970.
- [20] D. Dolan, "Accuracy and Precision in Photonic Doppler Velocimetry," *Review of Scientific Instruments*, vol. 81, no. 053905, 2010.
- [21] O. Strand and et al, "Velocimetry Using Heterodyne Techniques," *Review of Scientific Instruments*, vol. 77, no. 083108, 2006.
- [22] S. Dwivedi, "Two Dimensional Mesoscale Simulations of Projectile Instability During Penetration in Dry Sand," *Journal of Applied Physics*, vol. 104, no. 083502, 2008.
- [23] D. Fredenburg and N. Thadhani, "On the Applicability of the P-alpha and P-lambda Models to Describe the Dynamic Compaction Response of Highly Heterogeneous Powder Mixtures," *Journal of Applied Physics*, vol. 113, no. 043507, 2013.
- [24] D. Fredenburg, "Shock Compaction and Impact Response of Thermite Powder Mixtures," Georgia Institute of Technology, 2010.
- [25] D. Fredenburg and et al, "(U) Influence of Compaction Model Form on Planar and Cylindrical Compaction Geometries: LA-UR-18-20101," 2018.
- [26] H. Fischmeister and E. Arzt, "Densification of Powders by Particle Deformation," *Powder Metallurgy*, vol. 26, no. 2, 1983.
- [27] H. Fischmeister, "Powder Compaction: Fundamentals and Recent Developments," in *Proceedings of the Institution of Mechanical Engineers*, 1982.
- [28] E. Santiso and E. Muller, "Dense Packing of Binary and Polydisperse Hard Spheres," *Molecular Physics*, vol. 100, no. 3.1, 2002.

- [29] V. Kenkre and et al, "A Theoretical Model for the Compaction of Granular Materials," *Journal of the American Ceramics Society*, vol. 79, no. 12, 1996.
- [30] R. Abbaschian and et al, *Physical Metallurgy Principles*, Cengage Learning, 2010.
- [31] W. Herrmann, "Constitutive Equation for the Dynamic Compaction of Ductile Porous Materials," *Journal of Applied Physics*, vol. 40, pp. 2490 - 2499, 1969.
- [32] X. Xu and N. Thadhani, "Investigation of Shock-induced Reaction Behavior of As-blended and Ball-milled Ni + Ti Powder Mixtures Using Time-Resolved Stress Measurements," *Journal of Applied Physics*, vol. 96, no. 2000, 2004.
- [33] B. Butcher and C. Karnes, "Dynamic Compaction of Porous Iron," *Journal of Applied Physics*, vol. 40, pp. 2967-2976, 1969.
- [34] R. Boade, "Principal Hugoniot, Second-Shock Hugoniot, and Release Behavior of Pressed Copper Powder," *Journal of Applied Physics*, vol. 41, no. 11, 1970.
- [35] M. Carroll and A. Holt, "Suggested Modification of the P-alpha Model for Porous Materials," *Journal of Applied Physics*, vol. 43, pp. 759 - 761, 1972.
- [36] M. Carroll and A. Holt, "Static and Dynamic Pore-Collapse Relations for Ductile Porous Materials," *Journal of Applied Physics*, vol. 43, pp. 1626 - 1636, 1972.
- [37] R. Menikoff and E. Kober, "Equation of State and Hugoniot Locus for Porous Materials: P-alpha Model Revisited," *Shock Compression of Condensed Matter Conference Proceedings*, pp. 129 - 132, 1999.
- [38] D. Grady, "P-alpha Compaction of Sand," Sandia Internal Report.
- [39] J. Brown and et al, "Dynamic Compaction of Sand," in *Shock Compression of Condensed Matter - AIP Conference Proceedings*, 2007.
- [40] D. Fredenburg and et al, "Systematics of Compaction for Porous Metal and Metal-Oxide Systems," in *Shock Compression of Condensed Matter - AIP Conference Proceedings*, 2015.
- [41] B. Nolen, J. Wermer, D. Guidry and P. Pappin, "CeO<sub>2</sub> Sample Analysis," LANL MST-6, 2012.
- [42] "Los Alamos Neutron Science Center," Los Alamos National Laboratory, [Online]. Available: [lansce.lanl.gov](http://lansce.lanl.gov).
- [43] C. Morris and et al, "New Developments in Proton Radiography at the Los Alamos Neutron Science Center (LANSCE)," *Experimental Mechanics*, vol. 56, no. 1, 2016.

- [44] P. Turchi and et al, "PHELIX: Design and Analysis of a Transformer-Driver Liner Implosion System," *IEEE Transactions on Plasma Science*, vol. 39, no. 10, 2011.
- [45] C. Rousculp, "The PHELIX Pulsed Power Project: Bringing Portable Magnetic Drive to Proton Radiography," in *Magnetic Field Generation and Related Topics (MEGAGAUSS): 14th International Conference on Megagauss*, 2012.
- [46] D. Burton, "Lagrangian Hydrodynamics in the FLAG Code, LA-UR-07-7547," in *Symposium on Advanced Numerical Methods for Lagrangian Hydrodynamics*, 2007.
- [47] Shavano Project, *FLAG Code Manual*, 3.7.Alpha.4 ed., Los Alamos National Laboratory, 2017.
- [48] B. B. a. C. Karnes, "Dynamic Compaction of Porous Iron," *Journal of Applied Physics*, vol. 40, pp. 2967 - 2976, 1969.